npj | clean water

Article

Published in partnership with King Fahd University of Petroleum & Minerals

https://doi.org/10.1038/s41545-026-00599-y

# Integrated alkaline electrolyser-pressure retarded membrane distillation system for ammonia wastewater valorisation: technoeconomic and environmental assessment

Check for updates

Sunyoung Oh[1,3], Heun Se Kim[2,3], Kiho Park[2] ✉ & Boram Gu[1] ✉

Ammonia is a major wastewater pollutant causing eutrophication, and reliable removal across broad concentration ranges is increasingly required. However, conventional treatment processes are limited in operational stability, applicable concentration range and energy efficiency, while integrated approaches enabling simultaneous ammonia removal and resource recovery remain limited. This study proposes an integrated alkaline electrolyser (AEL) and waste-heat-driven pressure-retarded membrane distillation (PRMD), directly coupling ammonia electrolysis-based removal with hydrogen production, freshwater generation and energy recovery. A mathematical model incorporating mass and energy balances and pressure drop equations was developed alongside technoeconomic and environmental assessments over influent ammonia concentrations of 5–1000 ppm, a range broader than that typically considered for conventional ammonia treatment. The integrated AEL-PRMD system achieves stable ammonia removal while producing 99.9% pure hydrogen up to $1.22 \times 10^{-3}$ mol/s and $9.84 \times 10^{-6}$ $m^3$/s of freshwater. As ammonia concentration increases, the levelised cost of water rises from 5.5 to 12.4 $/m³, remaining comparable to thermal desalination, whereas environmental cost intensity decreases to 1.65 $/kg $CO_2$-eq at 1000 ppm. These results demonstrate stable ammonia removal and resource recovery across a wide concentration range. Overall, the integrated configuration redirects wastewater treatment energy into valuable co-products, providing a flexible and energy-efficient platform for ammonia wastewater valorisation.

Ammoniacal nitrogen in wastewater contributes to eutrophication, oxygen depletion and acidification. Such ammonia-containing wastewater is generated from diverse sources, including municipal wastewater treatment side-streams, landfill leachate, livestock and agricultural wastewater, anaerobic digestion effluents and various industrial wastewater streams. Accordingly, increasingly strict regulations require ammoniacal nitrogen removal to low concentrations, often below 10–20 ppm[1–3]. These regulatory pressures necessitate reliable and energy-efficient ammonia treatment technologies. Conventional approaches, including biological treatment, adsorption and air stripping (Table 1), are widely applied but exhibit limitations in operational stability, applicable concentration range or energy demand, with the corresponding wastewater types summarised in Supplementary Table S1. Consequently, advanced treatment technologies capable of maintaining stable performance while reducing operational complexity and energy consumption are required.

Electrochemical ammonia removal has recently attracted attention because it enables simultaneous wastewater treatment and hydrogen production. Previous studies have demonstrated that ammonia electrolysis can operate across a wide concentration range, from dilute secondary effluents to highly concentrated industrial streams[4–6]. However, despite this versatility, the reliance on direct electrical energy input remains a fundamental challenge.

[1]School of Chemical Engineering, Chonnam National University, Buk-gu, Gwangju, Republic of Korea. [2]Department of Chemical Engineering, Hanyang University, Seoul, Republic of Korea. [3]These authors contributed equally: Sunyoung Oh, Heun Se Kim. ✉e-mail: kiho138@hanyang.ac.kr; boram.gu@jnu.ac.kr

**Table 1 | A summary of the current ammonia removal technologies reported in the literature**

| Treatment methods | Process features | Scale | Ammonia loading capacity [ppm] | Removal efficiency [%] | Capacity [L/day] |
|---|---|---|---|---|---|
| Biological methods | Biological aerated filter system[84] | Lab. | 9.8 | 99.3 | 15 |
| | Partial nitritation system with biological selector[85] | Pilot | 2000 | 86.7 | 375 |
| | Upflow microaerobic membrane bioreactor[86] | Lab. | 200 | 96 | 4–8 |
| | Integrated nitrification-partial denitrification-anammox[87] | Pilot | 40–60 | 94.1 | 23.6 |
| | Recirculating vertical flow constructed wetlands[88] | Lab. | 450 | 87 | 6.7 |
| | **Advantages**: Simultaneous pollutant removal, sustainable nitrogen conversion, high removal efficiency at moderate loading<br>**Limitations**: Sensitive to dissolved oxygen and temperature, slow microbial kinetics, large reactor footprint, risk of clogging and $N_2O$ emission | | | | |
| Adsorption | Adsorption using zeolite, activated carbon and composite[89] | Lab. | 1890 | 78 | 0.1 |
| | Adsorption onto volcanic tuff[90] | Lab. | 200–300 | 85 | 2.4 |
| | Iron-loaded activated carbon adsorption[56] | Lab. | 5 | 85 | 0.24 |
| | Adsorption using modified bentonite[91] | Lab. | 168 | 71.7 | 1 |
| | Adsorption using natural zeolite[92] | Lab. | 200 | 85 | 2.4 |
| | **Advantages**: Rapid removal, simple operation, effective at low-to-moderate loading<br>**Limitations**: Sorbent saturation at high loading, regeneration/replacement cost, ionic competition and pH sensitivity | | | | |
| Air stripping | Columnar air stripping in a closed-loop system[93] | Pilot | 1158 | 98.5 | 960 |
| | Air stripping for municipal wastewater[57] | Lab. | 30-98 | 93 | 20 |
| | Slow rate ammonia stripping[94] | Pilot | 1580 | 69 | 100 |
| | Air stripping using a rotating packed bed[95] | Pilot | 1000 | 76 | 36 |
| | Combining ammonia stripping with struvite precipitation[96] | Lab. | 297 | 88 | 8 |
| | **Advantages**: Suitable for high-strength wastewater, operational robustness, high removal efficiency at elevated pH<br>**Limitations**: High energy demand, large gas-liquid contact area requirement, potential $NH_3$ emission and sludge generation | | | | |

Most existing studies on alkaline electrolyser (AEL) systems focus primarily on hydrogen production, evaluating performance mainly through electrochemical metrics such as catalyst activity, overpotential and current efficiency[7–11]. Although this approach provides valuable insights from a hydrogen production perspective, the broader implications for wastewater treatment remain insufficiently explored. As a result, AELs are often regarded as energy-intensive when evaluated solely as wastewater treatment technologies. This perception arises largely because electrical energy consumption is attributed exclusively to ammonia removal, neglecting the potential benefits of simultaneous resource generation.

In an AEL, ammonia is electrochemically oxidised at the anode under alkaline conditions, while hydrogen is produced at the cathode[4–6]. This enables ammonia removal to be directly coupled with hydrogen generation, although the practical feasibility of AEL-based wastewater treatment is strongly influenced by electrical energy demand. Pressure-retarded membrane distillation (PRMD) can provide complementary functions for ammonia wastewater valorisation when integrated with the AEL process. PRMD is a low-grade-heat-driven membrane process originally developed by combining direct contact membrane distillation (DCMD) and pressure-retarded osmosis (PRO), enabling membrane-distillation-based freshwater production to be coupled with pressure-retarded energy recovery[12]. Closed-loop PRMD was subsequently proposed to improve heat recovery by integrating a heat exchanger, thereby reducing external heat input and exergy destruction while maintaining water and electricity co-production[13]. More recently, solar-powered PRMD has been evaluated as a self-sustainable desalination system, showing the potential for water and energy production without external electricity under favourable solar conditions[14].

However, AEL and PRMD have predominantly been investigated as separate systems: electrochemical ammonia oxidation has demonstrated near-complete $NH_3$ removal (>99.8%)[15], while PRMD has demonstrated freshwater production and energy recovery based on water vapour flux ($13.27 \pm 0.72\ L/m^2/h$) and power density (up to $0.786\ W/m^2$)[16]. Their integration for simultaneous ammonia wastewater treatment, hydrogen production, freshwater generation and internal energy recovery has not yet been systematically evaluated.

To address this limitation, this study adopts a system-level perspective in which electrical energy input is leveraged to enable multiple simultaneous functions. Specifically, we propose an integrated process architecture that combines ammonia removal and hydrogen production with freshwater generation and energy recovery. The proposed system couples an AEL with a closed-loop PRMD unit, hereafter referred to as the integrated AEL-PRMD system. The AEL subsystem, which exhibits technological maturity, cost-effectiveness and high operational stability[17,18], performs electrochemical ammonia oxidation while producing hydrogen, whereas the PRMD subsystem utilises low-grade waste heat to generate freshwater and recover hydraulic energy[12]. PRMD pressurises the permeate produced by membrane distillation to drive a turbine, thereby generating electrical power. This internally generated electricity partially offsets the power demand of the electrolyser, improving overall electrical energy efficiency while enabling additional production of high-purity hydrogen and freshwater.

To evaluate the performance of this integrated architecture, a comprehensive system-level analysis of the integrated AEL-PRMD process is conducted. First, an integrated mathematical model incorporating mass and energy balances along with electrochemical reaction kinetics and membrane transport equations is developed to simulate the coupled AEL and PRMD units. This model is used to evaluate system performance over a wide range of influent ammonia concentrations (5–1000 ppm) while maintaining a target removal efficiency of 99.5%. Second, a system-level energy analysis is performed to quantify the net electrical requirement of the integrated process by accounting for internal energy recovery through the PRMD subsystem. Finally, the practical feasibility of the proposed system is assessed through technoeconomic analysis and life cycle assessment (LCA). These results are compared with conventional ammonia treatment technologies to evaluate the potential of the integrated AEL-PRMD system for achieving

stable wastewater treatment while simultaneously generating valuable resources.

Overall, this study establishes a comprehensive framework for analysing the integrated electrochemical-thermal processes for ammonia wastewater valorisation. By integrating the two unit processes, this framework goes beyond conventional wastewater treatment and reinterprets the energy used for ammonia removal as a pathway for value generation from a water-energy-environment nexus perspective. The results provide insight into how process integration, energy recovery and operating conditions influence treatment performance, resource recovery, economic viability and environmental sustainability, thereby supporting the future deployment of integrated AEL-PRMD systems for ammonia-rich wastewater treatment.

## Results and discussion

### Model validation

A comprehensive mathematical model of the integrated AEL and PRMD system was developed and validated separately for each subsystem model to ensure predictive reliability[12,16,19,20].

The AEL system for $NH_3$ electrolysis was validated against experimental data reported in the literature[16,20], as shown in Fig. 1.

As the $NH_3$ electrolysis model was adapted from the alkaline water electrolyser (AWE) framework proposed by Haug et al.[21], the base AWE model was first validated (Fig. S1 in Supplementary Note 2). The adapted $NH_3$ model was then validated using two independent datasets: (i) hydrogen generation data from Jiang et al.[19] (Fig. 1(a)) and (ii) cell voltage measurements at different temperatures from Van et al.[20] (Fig. 1(b)).

The model shows excellent agreement with experimental data, achieving an $R^2$ value of approximately 0.99 for hydrogen production. The voltage model was calibrated using temperature-dependent polarisation data, adjusting the charge transfer coefficient and reference exchange current density to capture electrode-specific kinetics. The resulting correlations accurately reproduce the experimental trends, as shown in Fig. 1(b), with the fitted parameters summarised in Table S2 (Supplementary Note 2).

The PRMD model was previously validated using water flux data in a dedicated study[12]. However, in the integrated AEL-PRMD system, higher permeate-side pressures are applied to enable electricity generation, which may affect membrane transport properties.

At elevated pressures, membrane deformation, characterised by reduced porosity, increased tortuosity and decreased pore size, can reduce permeability[16]. To account for this effect, pressure-dependent membrane permeance was incorporated through the inverse membrane resistance ($R_m$), as defined in Eq. (43). The model was calibrated using the experimental data reported by Yuan et al.[16], showing good agreement with observed pressure-permeance behaviour (Fig. 1(c)).

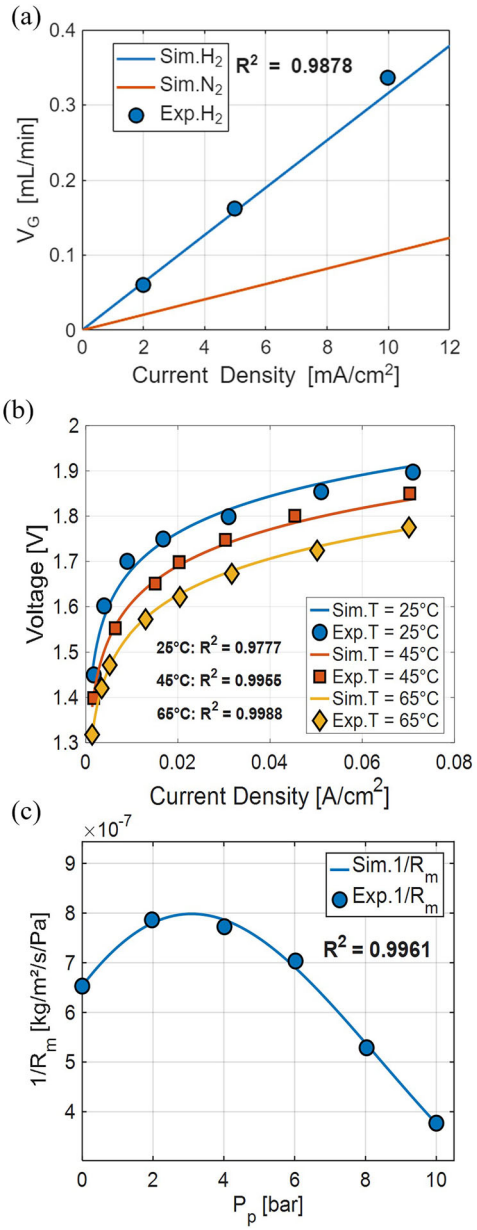



**Fig. 1 | Validation results for each subsystem of the integrated AEL-PRMD system. a** The $H_2$ generation rate was compared as a function of current density using $NH_3$ electrolysis data from Jiang et al.[19]. Blue circles indicate experimental data, while the blue and orange solid lines indicate simulated $H_2$ and $N_2$ production rates in our model, respectively, with $R^2 = 0.9878$ for $H_2$. **b** Cell voltage was compared over the current density range at different temperatures using experimental data from Van et al.[20]. Solid lines denote simulation results, and symbols denote experimental data; blue circles, orange squares and yellow diamonds correspond to 25, 45 and 65 °C, respectively, with $R^2 = 0.9777$, 0.9956 and 0.9988. **c** Pressure-dependent membrane permeability in the PRMD module was compared using experimental data from Yuan et al.[16]. Blue circles indicate literature data, and the blue solid line indicates the fitted model. $R_m$ denotes membrane resistance with $R^2 = 0.9961$ for the fitted model.

### Effect of AEL operating temperature on overall system performance

In the integrated AEL-PRMD system, electrical energy consumption in the AEL dominates the overall energy demand. Increasing the AEL operating temperature enhances electron transfer and ionic transport, reducing internal resistance and lowering electrical energy consumption[22–24]. However, excessively high temperatures may increase specific energy consumption due to $NH_3$ loss and side reactions[7,8,25]. In addition to affecting energy demand, AEL temperature also influences heat distribution and flow allocation within the PRMD module. Therefore, its impact on overall system performance is examined in this section.

To isolate the temperature effect, simulations were conducted using a single-stage configuration ($N_p = 1$) under fixed operating conditions (Table 6). The $NH_3$ concentrations in the produced freshwater and final treated effluent were also evaluated as indicators of both outlet-stream qualities. The $NH_3$ removal efficiency and $H_2$ purity were maintained at 99.5% and 99.9%, respectively (Table 2), and the results are presented in Fig. 2.

A decrease in total energy consumption with increasing AEL operating temperature is identified in Fig. 2(a), from 592 W at 25 °C to 547 W at 65 °C. Electrical energy accounts for more than 98% of total energy consumption across all cases, indicating that system performance is primarily governed by AEL operation. The observed reduction in total energy consumption is mainly attributed to decreased energy demand, while pumping energy and generated energy remain nearly constant, as illustrated in Fig. 2(d). This reduction can be explained by the temperature-enhanced electrochemical behaviour of the AEL, where improved charge transfer and ionic conductivity decrease activation and ohmic losses during ammonia electrolysis.

The variation in GOR identified in Fig. 2(b) reaches a minimum at 45 °C (GOR = 0.15), indicating that the thermal performance of the integrated system is strongly affected by the heat distribution between $HX_1$ and $HX_2$, as presented in Fig. 2(c). At 25 °C, all recovered heat is directed to $HX_2$, enabling efficient heating of the PRMD feed and minimising external heat input, resulting in the highest GOR (0.33). As the AEL operating temperature rises, a larger portion of the heated permeate is allocated to $HX_1$ to preheat the AEL feed, reducing the flow available to $HX_2$. Consequently, additional external heat is required to reach the target MD temperature, leading to a lower GOR.

At higher AEL temperatures (e.g., 65 °C), although the flow to $HX_2$ is reduced, the required heat duty is also lower due to the smaller temperature difference to the MD operation conditions. Therefore, the target temperature can be achieved with less supplementary heating compared to an intermediate temperature (45 °C), where the heat demand is highest.

A decreasing trend in the SEC for both hydrogen and freshwater production is identified with increasing AEL operating temperature, as indicated in Fig. 2(e). Since production rates remain constant across the cases, SEC follows the trend of total energy consumption shown in Fig. 2(a). The SEC for hydrogen production (0.12–0.13 kWh/mol) is higher than that of steam methane reforming (0.08–0.09 kWh/mol), the most widely used production technology[26], but avoids $CO_2$ emissions and additional purification requirements. The SEC for freshwater production (15.4–16.7 kWh/$m^3$) falls within the range of conventional thermal desalination processes such as multi-effect distillation (13.5–25.5 kWh/$m^3$)[27], indicating comparable desalination performance while simultaneously producing hydrogen.

Overall, within the investigated range, higher AEL operating temperatures improve system energy efficiency, although internal heat distribution and energy recovery remain strongly dependent on temperature.

**Table 2 | Summary of simulation results for three AEL temperatures, maintaining an $NH_3$ removal efficiency of 99.5% and an $H_2$ purity of 99.9%**

| Description | Symbol [unit] | Value |
|---|---|---|
| $H_2$ production rate | $n_{H2}$ [mol/s] | $1.22 \times 10^{-3}$ |
| $H_2$ purity | $y_{H2}$ [%] | 99.9 |
| Produced water amount | $V_{H2O}$ [$m^3$/s] | $9.84 \times 10^{-6}$ |
| $NH_3$ conc. in produced water | $C_{PW}$ [ppm] | 0.27 |
| $NH_3$ conc. in treated effluent | $C_{TE}$ [ppm] | 0.51 |
| Removal efficiency of $NH_3$ | $\eta_{NH3,rem}$ [%] | 99.5 |
| Water flux | $J_w$ [kg/$m^2$/s] | $7.17 \times 10^{-3}$ |
| $NH_3$ flux | $J_{NH3}$ [kg/$m^2$/s] | $2.01 \times 10^{-11}$ |

## Influence of influent ammonia concentration on system performance

To evaluate the applicability of the integrated AEL-PRMD system to different wastewater types, simulations were conducted for influent $NH_3$ concentrations of 5, 50, 500 and 1000 ppm, representing municipal, food processing, pharmaceutical and petrochemical wastewater, respectively. Key performance indicators are shown in Fig. 3.

The AEL operating temperature was fixed at 65 °C, which provided the highest energy efficiency as shown in the previous subsection. Operating conditions were adjusted to maintain an $NH_3$ removal efficiency of 99.5% (Tables 6 and 9). A two-stage PRMD configuration with six parallel modules was used based on the scale-up analysis (Figs. S2–S4 in Supplementary Note 3). The overall process-flow state is summarised in Table S3 following the

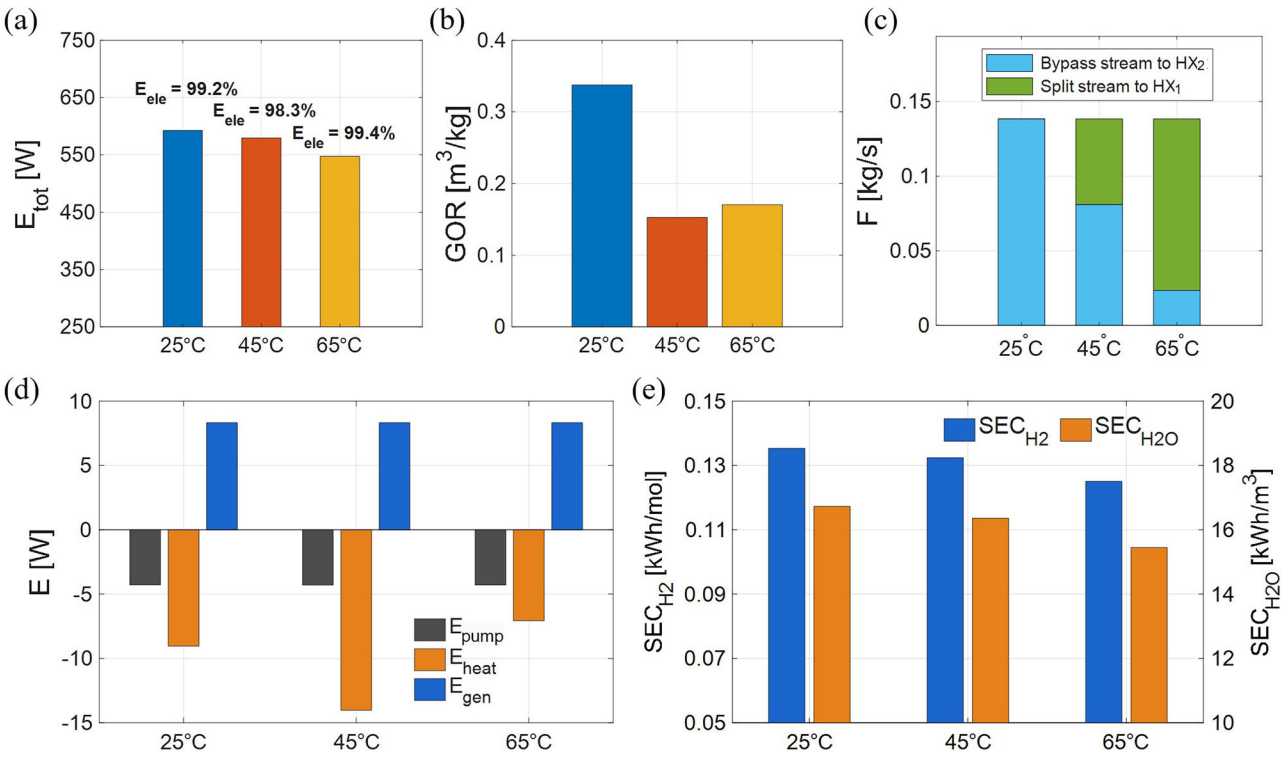



**Fig. 2 | Simulation results at different AEL operating temperatures.** Results are obtained for AEL operating temperatures of 25, 45 and 65 °C. **a** The total energy consumption of the integrated AEL-PRMD system is shown as a bar chart, and the percentage above each bar indicates the fraction of AEL electrical energy in the total energy consumption. **b** The GOR used to calculate the supplied heat is shown as a bar chart. **c** The flow allocation of the permeate-side stream for achieving the target MD operating temperature is shown as a stacked bar chart, where blue indicates the bypass stream to $HX_2$ and green indicates the split stream supplied to $HX_2$ after $HX_1$. **d** Blue represents the pump energy requirement, orange represents the supplied heat and yellow represents the electrical energy generated by the hydro-turbine. Negative values indicate energy consumption, whereas positive values indicate energy generation. **e** Blue represents the specific energy consumption for hydrogen production, and orange represents the specific energy consumption for freshwater production.

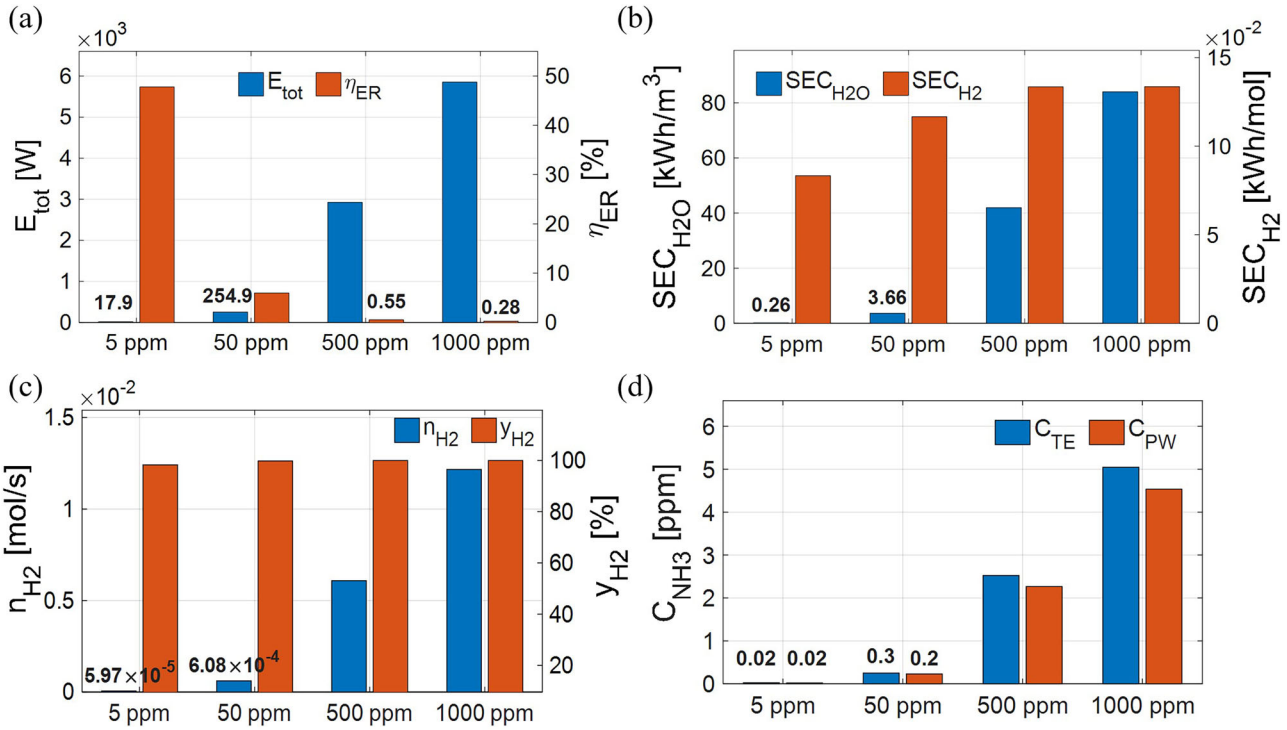



**Fig. 3 | Simulation results for different influent $NH_3$ concentrations.** The simulation results are shown for influent $NH_3$ concentrations of 5, 50, 500 and 1000 ppm. **a** Total energy consumption and generated energy ratio, with blue representing total energy consumption and red representing the generated energy ratio. **b** Specific energy consumption for hydrogen and freshwater production, with blue representing freshwater production and red representing hydrogen production. **c** Hydrogen production rate and hydrogen purity, with blue representing hydrogen production rate and red representing hydrogen purity. **d** $NH_3$ concentration in the outlet streams, with blue representing the final treated effluent discharged after the MD module and red representing the produced freshwater recovered after passing through the hydro-turbine. Values that are difficult to distinguish because of small bar heights are labelled above the corresponding bars.

flow sequence shown in Fig. S5. The removal efficiency was selected to ensure regulatory compliance. Lower efficiencies (90-95%) reduce energy consumption but may result in effluent and product water $NH_3$ concentrations exceeding typical discharge limits (<20 ppm[2,28,29]) (Fig. S6, Supplementary Note 3).

A substantial increase in total energy consumption with influent $NH_3$ concentration is identified in Fig. 3(a), rising from 18 W at 5 ppm to 5851 W at 1000 ppm. This increase is driven by the higher electrical demand required in the AEL to achieve the fixed removal efficiency. As a result, the SEC for both hydrogen and freshwater increases, as observed in Fig. 3(b). The increase in freshwater SEC is particularly pronounced because freshwater production remains nearly constant (~$1.92 \times 10^{-5}$ $m^3/s$), while energy consumption rises substantially.

The hydrogen production rate presented in Fig. 3(c) increases almost linearly with influent $NH_3$ concentration, from $5.97 \times 10^{-5}$ to $1.21 \times 10^{-3}$ $m^3/s$. This increase is closely associated with the rise in total energy consumption presented in Fig. 3(a), as a higher $NH_3$ loading requires greater electrochemical reaction throughput and electrical energy input in the AEL. Hydrogen purity improves from 98.3% at 5 ppm to ~99.99% above 500 ppm, with only marginal gains at higher concentrations. The increase in $H_2$ purity with influent $NH_3$ concentration can be attributed to the larger $H_2$ generation rate at the cathode, which reduces the relative contribution of $N_2$ crossover-derived impurities in the outlet gas stream.

Figure 3(d) presents the $NH_3$ concentrations in the treated effluent and produced freshwater. With a fixed removal efficiency of 99.5%, residual $NH_3$ concentration increases proportionally with influent concentration. Slight $NH_3$ permeation into the permeate stream is observed due to increased partial-pressure differences; however, effluent concentrations remain below 10 ppm across all cases, satisfying regulatory limits[29].

Overall, higher $NH_3$ concentrations improve hydrogen production but significantly increase energy consumption, whereas very low concentrations result in limited hydrogen recovery. Therefore, the integrated AEL-PRMD system is most suitable for moderate $NH_3$ concentrations, where hydrogen production is meaningful without excessive energy demand.

## Comparison with conventional technologies

The performance of the integrated AEL-PRMD system is compared with conventional technologies in terms of energy consumption for wastewater treatment and resource recovery. The comparison is based on SEC, enabling consistent evaluation across different process configurations. It should be noted that this comparison is intended as functional benchmarking rather than a direct one-to-one ranking of overall process superiority. Because the integrated AEL-PRMD system produces multiple outputs, whereas most conventional technologies are designed for a single primary function, each panel uses an output-specific SEC: $SEC_{ww}$ for treated wastewater volume, $SEC_{H2}$ for hydrogen production volume and $SEC_{H2O}$ for freshwater production volume. The SEC of the integrated AEL-PRMD system was calculated using the results from 12 operating conditions presented in Fig. S6 of Supplementary Note 3, covering influent $NH_3$ concentrations of 5–1000 ppm and $NH_3$ removal efficiencies of 90%, 95% and 99.5%; the corresponding error bar represents the minimum-to-maximum range of these values.

Figure 4(a) compares the SEC of the integrated AEL-PRMD system with conventional wastewater treatment technologies. The reported values are literature data from laboratory- and full-scale systems, with average values shown as bars and ranges indicated by error bars (see Tables S4 and S5 in Supplementary Note 4). Conventional biological processes, such as conventional activated sludge (CAS) and the anoxic-anaerobic-oxic (A2O), exhibit relatively low SEC because $NH_3$ removal is driven by aeration-supported microbial nitrification rather than direct electrochemical oxidation[30–32]. However, their energy demand increases under stricter effluent standards due to higher aeration requirements. Membrane

bioreactor (MBR) systems require additional energy for aeration and fouling control[33,34], while adsorption processes incur energy penalties associated with adsorbent regeneration[35,36].

Figure 4(b, c) compare the SEC of the integrated AEL-PRMD system with conventional hydrogen production and desalination technologies. Literature data were compiled from laboratory-scale experiments, industrial systems and simulation studies, with average values shown as bars and reported ranges indicated by error bars (see Tables S6 and S7 in the Supplementary Note 4 for details).

For hydrogen production (Fig. 4(b)), the SEC of the integrated AEL-PRMD system (3.63–5.96 kWh/Nm$^3$, average ~5.18 kWh/Nm$^3$) falls within the range of electrolysis-based technologies. Laboratory-scale $NH_3$ electrolysis benefits from a lower thermodynamic equilibrium potential than water electrolysis (1.23 vs 0.08 V), resulting in lower theoretical energy demand at ~2.71 kWh/Nm$^3$ [25,37–40], while conventional water electrolysis technologies AWE (~4.91 kWh/Nm$^3$) and proton exchange membrane (PEM) electrolysis exhibit a wide SEC range depending on system design and operating conditions[41].

For freshwater production (Fig. 4(c)), the integrated AEL-PRMD system exhibits an average SEC of 30.9 kWh/m$^3$, with a wide range of 0.23–84.02 kWh/m$^3$ depending on influent $NH_3$ concentration and removal requirements. Thermal desalination processes such as multi-effect distillation (MED) and multi-stage flash (MSF) show higher equivalent electrical energy consumption due to phase change requirements, with MSF reaching up to ~124 kWh/m$^3$ [27,42–44]. In contrast, membrane-based processes such as reverse osmosis (RO) and nanofiltration (NF) demonstrate significantly lower SEC values (4.4–4.6 kWh/m$^3$) due to pressure-driven separation[45–48].

The higher $SEC_{ww}$ of the integrated AEL-PRMD system reflects the additional energy required for electrochemical $NH_3$ removal and simultaneous resource generation. Therefore, Fig. 4 should not be interpreted as demonstrating that the integrated AEL-PRMD system outperforms all conventional technologies in every individual energy metric. Rather, the comparison positions the proposed system relative to established single-purpose technologies under output-specific SEC criteria, while its overall value should be assessed together with multifunctional outputs, internal energy recovery and the TEA-LCA results.

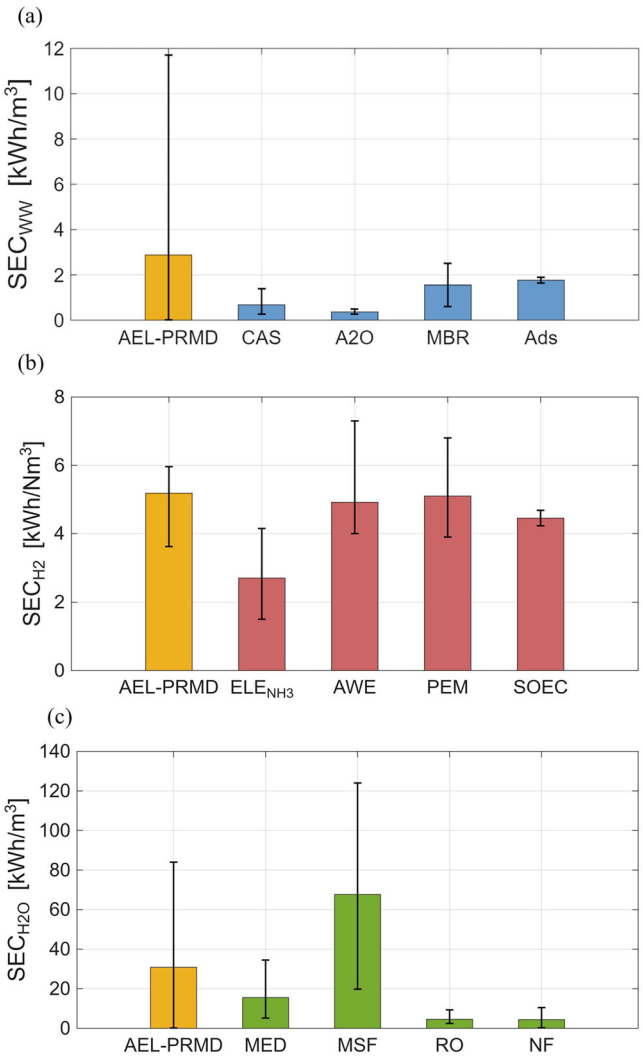



**Fig. 4 | Comparison of SEC for the integrated AEL-PRMD system and conventional technologies.** Output-specific energy consumption is compared across wastewater treatment, hydrogen production and desalination technologies based on literature data compiled in Supplementary Note 4. Bars indicate average values, and error bars indicate minimum-to-maximum ranges. **a** SEC comparison for wastewater treatment, including conventional activated sludge (CAS), anaerobic-anoxic-oxic (A2O), membrane bioreactor (MBR) and adsorption (Ads). **b** SEC comparison for hydrogen production, including ammonia electrolysis ($ELE_{NH3}$), alkaline water electrolysis (AWE), proton exchange membrane electrolysis (PEM) and solid oxide electrolysis cell (SOEC). **c** SEC comparison for freshwater production, including multi-effect distillation (MED), multi-stage flash (MSF), reverse osmosis (RO) and nanofiltration (NF).

## Cost analysis

From an economic perspective, wastewater treatment (i.e., ammonia removal) represents the primary function of the integrated AEL-PRMD system. Therefore, cost is evaluated as the unit treatment cost, defined as the annualised system cost divided by the annual treated wastewater volume. This is compared with reported costs for conventional wastewater treatment, including RO-based processes, hybrid membrane systems (forward osmosis (FO), RO and anaerobic membrane bioreactor (AnMBR) and conventional treatment plants[49–51], summarised in Table 3.

The lowest cost is obtained at 5 ppm (0.65 €/m$^3$), increasing to 1.45 €/m$^3$ at 1000 ppm. At low concentrations (5–50 ppm), the cost is lower than RO polishing (0.87 €/m$^3$) and comparable to hybrid FO-RO-AnMBR systems (0.81–1.27 €/m$^3$). This increase is mainly caused by the higher electrical cost associated with the larger AEL current requirement at higher $NH_3$ loading, while the treated wastewater volume remains fixed in the unit-cost calculation. At higher concentrations, the cost exceeds RO polishing but remains comparable to the integrated RO-based treatment process (1.57 €/m$^3$).

Although the integrated AEL-PRMD system does not always provide the lowest treatment cost, its economic performance should be interpreted within a multifunctional framework rather than compared solely with single-purpose treatment technologies.

The economic assessment was performed to examine how influent $NH_3$ concentration affects the production costs of the co-products from the integrated AEL-PRMD system. Figure 5 presents the levelised cost of water (LCOW), electricity (LCOE) and hydrogen (LCOH) for the integrated AEL-PRMD system across influent ammonia concentrations of 5–1000 ppm. As shown in Fig. 5(a), LCOW rises with $NH_3$ concentration, from 5.5 $/m$^3$ at 5 ppm to 12.4 $/m$^3$ at 1000 ppm. This trend reflects that an increase in total energy consumption is required to achieve the target $NH_3$ removal (Fig. 3). Under dilute conditions (≤50 ppm), LCOW remains relatively low (5.5–5.8 $/m$^3$) due to reduced electricity demand and partial offset by PRMD energy recovery.

The increase in LCOE with $NH_3$ concentration, from 23.7 to 52.9 $/kWh, is presented in Fig. 5(b). PRMD electricity generation remains nearly constant (~16 W), providing only a limited offset to the increasing power demand of the AEL. At 5 ppm, approximately 47% of the total electricity demand is offset, whereas the offset becomes negligible at higher concentrations (~6% at 50 ppm). Consequently, LCOE is primarily governed by the concentration-dependent increase in AEL electricity consumption, as also shown in Fig. 5(a).

**Table 3 | Comparison of unit wastewater treatment cost**

| Process type | Process details | Purpose | Unit treatment cost | Reference |
|---|---|---|---|---|
| Conventional | RO | Wastewater treatment | 0.87 €/m$^3$ | 51 |
| | Integrated RO process | Secondary treatment | 1.57 €/m$^3$ | 51 |
| | FO-RO AnMBR | Municipal wastewater treatment | 0.81–1.27 €/m$^3$ | 50 |
| | Secondary treatment WWTP | Municipal wastewater treatment | 0.41–0.77 €/m$^3$ | 49 |
| Integrated AEL-PRMD | | - | 0.65–1.45 €/m$^3$ | Our study |

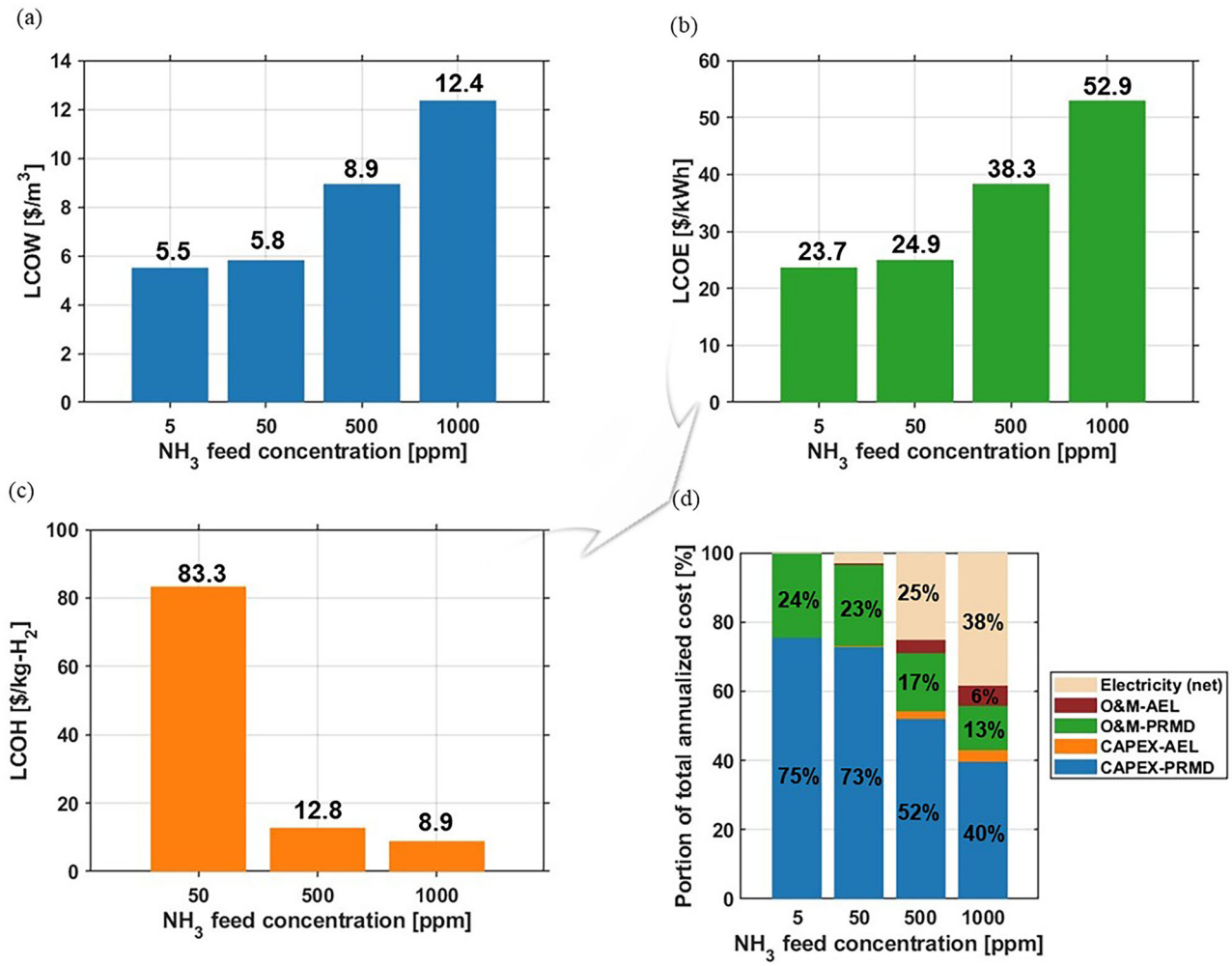



**Fig. 5 | Levelised cost analysis of the integrated AEL-PRMD system under varying influent ammonia concentrations. a** Levelised cost of water (LCOW) based on produced freshwater. **b** Levelised cost of electricity (LCOE) based on electricity generated by PRMD. **c** Levelised cost of hydrogen (LCOH) based on hydrogen produced by AEL. **d** Cost breakdown of the total annualised cost used for LCOW calculation, where blue represents CAPEX-PRMD, orange represents CAPEX-AEL, green represents O&M-PRMD, red represents O&M-AEL and light beige represents net electricity cost. The numbers inside the bars indicate the contribution of each cost component to the total annualised cost.

The LCOH is estimated to be extremely high at approximately 809.9 $/kg-$H_2$ at 5 ppm owing to the limited hydrogen production of approximately 4.1 kg/yr, indicating the strong sensitivity of LCOH to ammonia concentration, as presented in Fig. 5(c). Therefore, this condition was excluded from meaningful comparison. In the range of 50–1000 ppm, LCOH decreases substantially from 83.3 to 8.9 $/kg-$H_2$, reflecting increased hydrogen production that distributes the fixed capital and operating costs over a larger output.

Figure 5(d) presents the cost composition of the total annualised cost used for LCOW calculation. At low concentrations (5–50 ppm), PRMD-related CAPEX dominates (~75% of the total cost), while electricity contribution is minimal (<3%). As concentration increases, electricity becomes a major cost component, reaching ~38% at 1000 ppm, due to increased AEL energy demand. In contrast, O&M costs vary only slightly, indicating that cost escalation at high concentrations is primarily attributed to electricity consumption.

Overall, the integrated AEL-PRMD system is most economically favourable at low to moderate ammonia concentrations, where net electricity demand remains limited. At higher concentrations, cost increases are mainly dominated by AEL energy requirements, although internal energy recovery still provides partial mitigation.

**Table 4 | Comparison of levelised cost for the integrated AEL-PRMD system under varying wastewater desalination processes**

| Recovered resource | Process | Symbol [unit] | Value [Source] |
|---|---|---|---|
| Freshwater | NF | LCOW [$/m$^3$] | 0.08–0.12[97] |
| | RO | LCOW [$/m$^3$] | 0.45–6.56[98] |
| | MD | LCOW [$/m$^3$] | 4.57–24.61[97] |
| | ED | LCOW [$/m$^3$] | 0.3–10[99] |
| | MVR | LCOW [$/m$^3$] | 22–39[97] |
| | HDH | LCOW [$/m$^3$] | 10.8–98.1[100,101] |
| | MSF | LCOW [$/m$^3$] | 0.9–1.5[102] |
| | FO | LCOW [EUR/m$^3$] | 2.5[103] |
| | PRMD | LCOW [$/m$^3$] | 8.91–14.69[14] |
| Electricity | PRMD | LCOE [$/kWh] | 20.56–32.74[14] |
| Hydrogen | PEM | LCOH [€/kg-$H_2$] | 7.91[104] |
| Freshwater, electricity, hydrogen | Integrated AEL-PRMD (Our study) | LCOW [$/m$^3$] | 5.5–12.4 |
| | | LCOE [$/kWh] | 23.7–52.9 |
| | | LCOH [$/kg-$H_2$] | 8.9–809.9 |

Table 4 compares the levelised costs of the integrated AEL-PRMD system with representative desalination and hydrogen production technologies. The LCOW range (5.5–12.4 $/m$^3$) is higher than pressure-driven processes such as NF and RO, but falls within the range of thermal desalination technologies (e.g., MD and humidification-dehumidification (HDH) and overlaps with reported PRMD values. This reflects additional energy required for electrochemical $NH_3$ removal rather than limitations of the desalination subsystem itself. For electricity, the LCOE (23.7–52.9 $/kWh) is comparable to the PRMD-based system at low concentrations, but increases significantly at higher concentrations due to rising AEL electricity demand. For hydrogen, LCOH decreases with concentration and reaches values comparable to proton exchange membrane (PEM) electrolysis (~7.91 €/kg-$H_2$) at high concentrations. This indicates that hydrogen production becomes economically competitive when sufficient $NH_3$ is available, although performance remains constrained by wastewater treatment requirements. This cost behaviour reflects a shift in the dominant economic driver from limited product output at low $NH_3$ concentration to electricity-intensive ammonia oxidation at high $NH_3$ concentration.

## LCA of the AEL-PRMD system

The environmental performance of the integrated AEL-PRMD system was evaluated for influent $NH_3$ concentration of 5–1000 ppm using the ReCiPe 2016 (H) method. Selected midpoint indicators (global warming, marine ecotoxicity, freshwater eutrophication, human toxicity, ozone formation and fossil resource scarcity) and the corresponding endpoint indicators (human health, ecosystems and resources) were analysed to assess concentration-dependent impacts. In addition to the integrated system, standalone AEL and PRMD subsystems were evaluated to quantify the effect of process integration on environmental performance.

The midpoint and endpoint results were first analysed to assess how the environmental impacts vary with influent $NH_3$ concentration. Across all scenarios, normalised midpoint indicators show a clear concentration-dependent trend. Energy-related categories—global warming, fossil resource scarcity and human toxicity—increase most significantly with influent $NH_3$ concentration. This behaviour is consistent with the energy analysis, as higher $NH_3$ concentrations require greater electrical input for electrochemical oxidation, increasing upstream emissions associated with electricity supply.

As shown in Fig. 6(a), human toxicity exhibits the highest normalised impact among all categories, whereas freshwater eutrophication and ozone formation remain comparatively low. This is due to the strong dependence of the system on electricity consumption, particularly emissions from combustion-based power generation (e.g., $NO_x$, $SO_x$, particulate matter and heavy metals)[52]. Absolute midpoint results show that human toxicity increases from 14.9 to 23.3 kg 1,4-DCB-eq as $NH_3$ concentration increases from 5 ppm to 1000 ppm. Similar trends are observed for global warming (3.48–5.38 kg $CO_2$-eq) and fossil resource scarcity (0.92–1.41 kg oil-eq), confirming that environmental impacts are primarily driven by electricity demand rather than direct nutrient emissions.

The endpoint results shown in Fig. 6(b) show that human health and resource scarcity impacts remain comparable across the entire concentration range, with only minor differences between the two. In contrast, ecosystem damage is consistently much lower and exhibits only slight variation with influent concentration, indicating limited sensitivity to concentration changes.

The results reveal that system performance is strongly dependent on influent ammonia concentration, with distinct trade-offs between energy, economic and environmental metrics. Dilute conditions ( ≤ 50 ppm) provide the highest energy efficiency and lowest wastewater treatment cost, whereas moderate-to-high concentrations ( > 500 ppm) significantly enhance hydrogen productivity and economic viability. Under the investigated conditions, the specific energy consumption reaches up to 5.96 kWh/m$^3$, while hydrogen production increases by more than an order of magnitude across the concentration range. Although electricity demand increases with ammonia concentration, the model predicts stable treatment and resource recovery performance across the investigated concentration range.

The environmental benefit of process integration was further evaluated by comparing the integrated AEL-PRMD system with standalone AEL and PRMD subsystems. For global warming potential (GWP) (Fig. 7(a)), the standalone AEL exhibits the highest impact (4.187 kg $CO_2$-eq) due to its dependence on grid electricity, whereas the standalone PRMD has a much lower GWP (0.304 kg $CO_2$-eq) due to its thermally driven operation. The integrated system reduces GWP by 17% at low concentration (5 ppm) compared to the standalone AEL, reflecting partial substitution of grid electricity by internally recovered energy. At higher concentrations, the difference becomes smaller as AEL electricity demand increases, e.g., at 1000 ppm, 5.382 kg $CO_2$-eq for the integrated system vs 5.375 kg $CO_2$-eq for the standalone AEL.

A similar trend is observed for human health impacts (Fig. 7(b)), where the integrated AEL-PRMD reduces impacts relative to the standalone AEL, particularly under dilute conditions. For ecosystem damage (Fig. 7(c)) and resource scarcity (Fig. 7(d)), the integrated system consistently shows lower impacts than the standalone AEL, although the relative improvement decreases at higher concentrations.

For all LCA indicators presented in Fig. 7(a–d), environmental impacts increase with influent $NH_3$ concentration due to increased electricity demand in the AEL. The benefit of integration arises from internal energy recovery in the PRMD unit, which reduces reliance on grid electricity. However, this benefit diminishes at high concentrations as AEL energy demand increases more rapidly than the recovered energy.

Overall, the integrated AEL-PRMD system can reduce electricity-related environmental burden compared with standalone electrochemical treatment while maintaining multifunctional performance.

## Environmental cost intensity (ECI)

Table 5 summarises the ECI of the integrated AEL-PRMD system across influent ammonia concentrations of 5–1000 ppm, based on the ratio of annualised hydrogen production cost $C_{ann,H_2}$ to the annual global warming potential $GWP_{ann}$ (Eq. (89)).

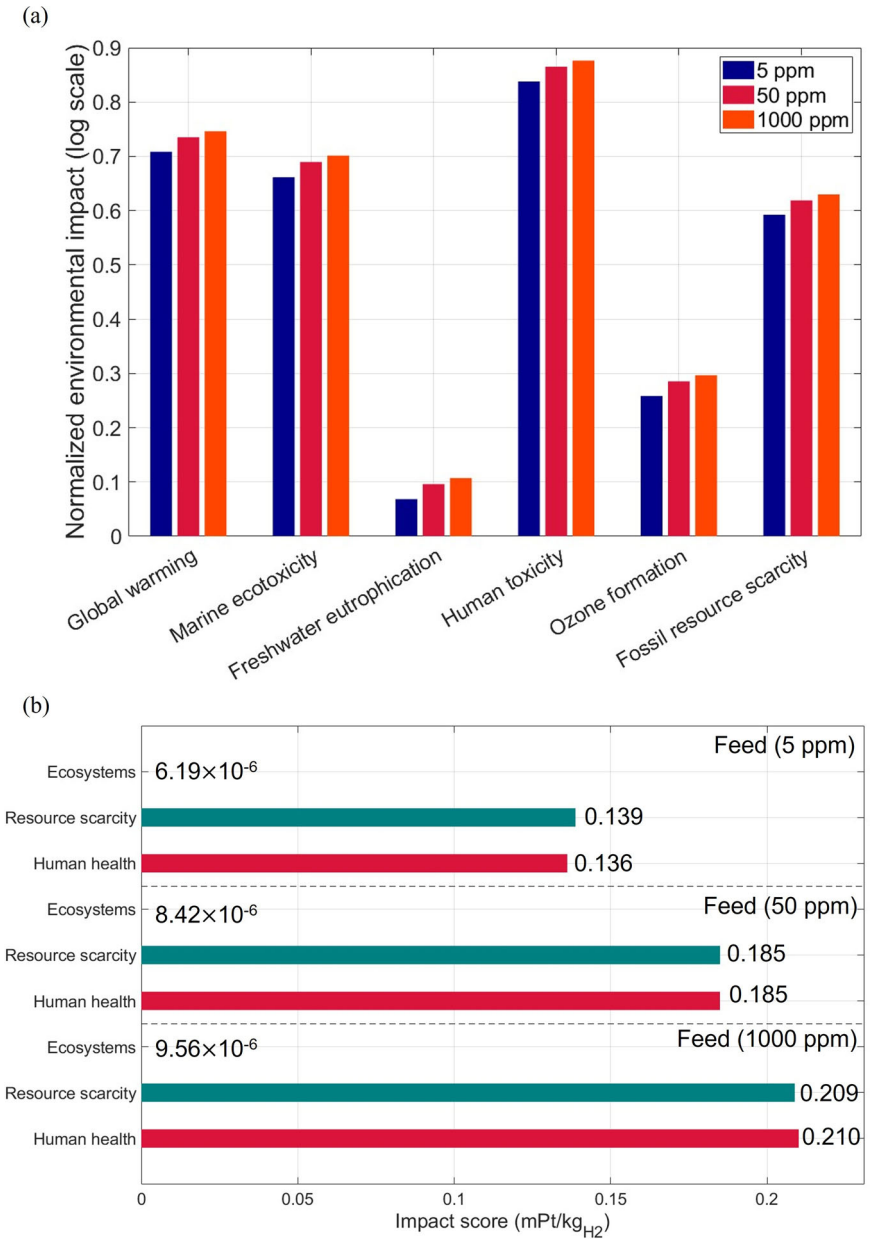



**Fig. 6 | Environmental impact of ammonia wastewater feed concentration. a** Normalised midpoint impacts calculated using the ReCiPe 2016 (H) method, including global warming, marine ecotoxicity, freshwater eutrophication, human toxicity, ozone formation and fossil resource scarcity. Navy blue, red and orange bars represent influent $NH_3$ concentrations of 5, 50 and 1000 ppm, respectively. **b** Endpoint impacts at 5, 50 and 1000 ppm, derived from the midpoint outcomes and grouped into human health, ecosystems and resource scarcity categories. The numbers beside the bars indicate the impact scores for each endpoint category.

As shown in Table 5, $C_{ann,H_2}$ increases moderately with influent concentration (3074–6885 $/yr), whereas $GWP_{ann}$ increases by several orders of magnitude (13.2–4163 kg $CO_2$-eq/yr) due to the strong increase in annual hydrogen production. Consequently, ECI decreases from 233 to 1.65 $/kg $CO_2$-eq as influent concentration increases. This trend indicates that, at higher-strength ammonia concentrations, the system achieves a lower cost per unit climate impact on an annual basis, primarily because a larger ammonia load is processed and converted into hydrogen under similar hydraulic recovery and auxiliary requirements. This behaviour suggests that higher $NH_3$ loading improves system utilisation by increasing the amount of recoverable hydrogen produced within the same integrated process configuration.

However, this reduction in ECI does not imply a lower absolute environmental impact. As discussed in *Cost analysis* and *LCA of the AEL-PRMD system*, both treatment cost and environmental burdens increase with ammonia concentration due to higher electricity demand in the AEL. The decreasing ECI reflects that the annual climate burden increases more rapidly than the associated cost as hydrogen productivity increases.

Therefore, ECI should be interpreted as a complementary indicator capturing the trade-off between economic cost and environmental impact. The selection of optimal operating conditions should consider absolute impacts, treatment performance and operational feasibility, in addition to ECI. Overall, the ECI analysis highlights the system-level value of the integrated AEL-PRMD configuration, where wastewater treatment is coupled with resource recovery, improving cost-impact efficiency at higher ammonia concentrations.

From an economic perspective, the integrated system achieves competitive wastewater treatment costs (0.65-1.45 €/$m^3$) and enables economically favourable hydrogen production at higher concentrations, with LCOH decreasing to approximately 8.9 $/kg. Environmentally, the system is primarily governed by electricity-related impacts; however, the environmental cost intensity (ECI) decreases from 233 to 1.65 $/kg $CO_2$-eq as concentration increases, reflecting improved cost-to-climate efficiency due to increased resource recovery. These results highlight that optimal operation depends not on a single performance metric, but on the targeted balance between treatment, resource recovery and sustainability objectives.

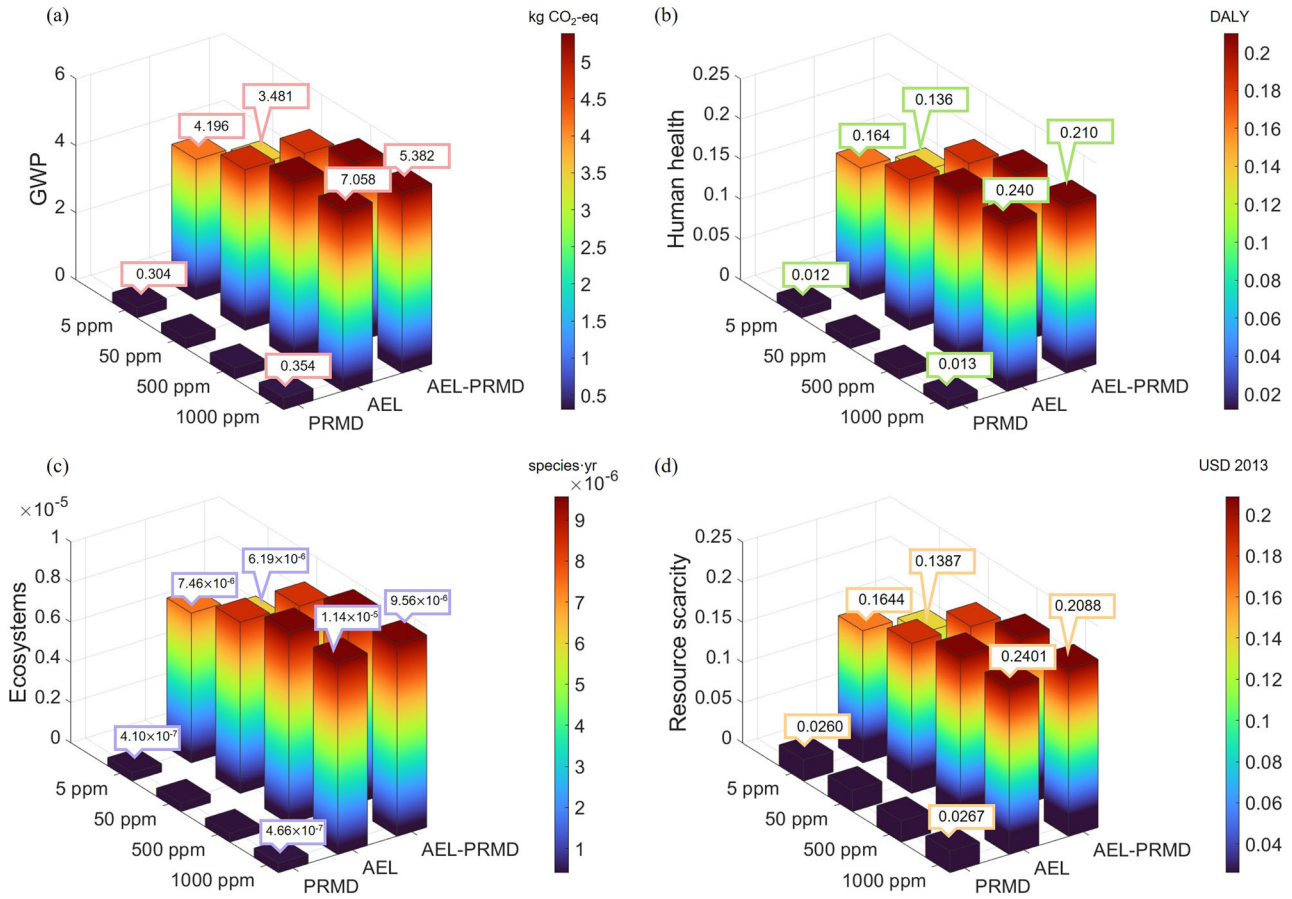



**Fig. 7 | Comparative environmental impacts of the standalone AEL, standalone PRMD and integrated AEL-PRMD systems under varying influent ammonia concentrations.** The LCA results are shown for influent $NH_3$ concentrations of 5, 50, 500 and 1000 ppm. **a** Global warming potential (GWP, kg $CO_2$ eq), (**b**) Human health impact (DALY). **c** Ecosystem (species·yr). **d** Resource scarcity (USD 2013). The height of each 3D bar indicates the impact value, and the colour scale represents the impact magnitude in the unit shown for each panel. The labels above the bars provide the numerical values for each condition.

**Table 5 | Comparison of unit wastewater treatment cost, GWP and ECI for the integrated AEL-PRMD system under varying ammonia concentrations and conventional desalination processes**

| Indicators | $NH_3$ concentration | | | |
|---|---|---|---|---|
| | 5 ppm | 50 ppm | 500 ppm | 1000 ppm |
| $GWP_{FU}$ [kg $CO_2$-eq/kg $H_2$-eq] | 3.48 | 4.73 | 5.38 | 5.38 |
| $H_{2_{gen}}$ [kg-$H_2$/yr] | 3.80 | 38.7 | 387 | 774 |
| $GWP_{ann}$ [kg $CO_2$-eq/yr] | 13.2 | 183 | $2.08 \times 10^3$ | $4.16 \times 10^3$ |
| LCOH [$/kg-$H_2$] | 809.9 | 83.3 | 12.8 | 8.9 |
| $C_{ann,H_2}$ [$/yr] | $3.07 \times 10^3$ | $3.22 \times 10^3$ | $4.95 \times 10^3$ | $6.89 \times 10^3$ |
| ECI [$/kg $CO_2$-eq] | 233 | 17.6 | 2.38 | 1.65 |

**Practical implications and future perspectives.** This study proposes and evaluates the integrated AEL-PRMD system that combines electrochemical ammonia removal with simultaneous hydrogen production and freshwater generation. By integrating an alkaline electrolyser with a waste-heat-driven PRMD unit, the system enables internal energy circulation, where recovered hydraulic energy partially offsets electricity demand. This integrated configuration provides a multifunctional platform that couples wastewater treatment with resource recovery. However, the fully integrated system was not experimentally validated in this study, and the following additional considerations are required for practical application to real industrial wastewater.

First, the analysis assumed a post-pretreatment wastewater condition to focus on the core performance of the integrated AEL-PRMD system. In practical applications, residual solids, organic matter and scaling-forming species may affect electrode reactions, membrane fouling and long-term stability[53–55]. Future studies should therefore include wastewater-specific pretreatment and assess its energy, chemical and cost implications.

Second, simulated wastewater centred on $NH_3/NH_4^+$ was used to focus the analysis on the effects of ammonia concentration, pH and temperature. While this approach is consistent with previous ammonia removal and recovery studies, it does not fully represent real-wastewater composition[4,56–58]. Since real wastewater may contain additional buffering and ionic species, future studies should validate the integrated AEL-PRMD system using representative post-pretreatment wastewater compositions or real municipal side-streams.

Finally, further validation is required for the scale-up and long-term operational stability of the integrated AEL-PRMD system. Practical implementation may be affected by membrane and electrode stability, fouling control, pressure conditions and module design. Therefore, future work should use the integrated mathematical model to screen key operating and design ranges, followed by long-term operation tests, real-wastewater validation and pilot-scale module assessment. Such validation would support the practical development and scale-up of integrated electrochemical-thermal treatment systems, thereby strengthening the basis for coupling wastewater treatment with water–energy–resource recovery.

## Methods

### Integrated system architecture and assessment framework

The integrated AEL-PRMD system combines an AEL with a PRMD unit, together with two heat exchangers ($HX_1$ and $HX_2$), three pumps (Pumps 1 to 3) and a hydro-turbine (HT), as illustrated in Fig. 8. The feed wastewater containing ammonia was assumed to be a pretreated ammonia-containing stream in which suspended solids and precipitable impurities had been removed upstream; therefore, only dissolved ammonia and ammonium species were considered to focus on ammonia-nitrogen removal.

In the integrated system, feed wastewater containing ammonia ($NH_3$) is first supplied to the AEL, where $NH_3$ is electrochemically oxidised to nitrogen ($N_2$) while hydrogen ($H_2$) is produced at the cathode. The AEL effluent, containing residual $NH_3$, is then heated to ~80 °C and delivered to the PRMD module. In the PRMD, a temperature gradient across the hydrophobic membrane drives vapour transport, producing freshwater and a treated retentate stream. The pressurised permeate stream is expanded through the HT to recover hydraulic energy into electricity. Through this integration, the system simultaneously achieves $NH_3$ removal, $H_2$ production, freshwater generation and partial electricity recovery.

Energy integration is achieved through two energy coupling strategies. First, electricity generated by the HT is used to offset part of the AEL power demand. Second, heat from the PRMD permeate stream (with ~83 °C) is recovered through $HX_1$ and $HX_2$. The heated permeate first preheats the AEL feed in $HX_1$, and the remaining stream is directed to $HX_2$ to raise the PRMD feed temperature, because higher AEL temperatures can improve splitting efficiency[22–24]. If the outlet temperature after $HX_2$ remains below the target MD operating temperature (~90 °C), supplementary external heating is applied. This configuration minimises external heating demand for the AEL feed and reduces the thermal duty required for PRMD operation.

This study presents a comprehensive system-level evaluation of the integrated AEL-PRMD process, combining process modelling with energy, economic and environmental assessments. The framework is designed to clarify how process integration and internal energy coupling influence treatment performance, resource recovery and sustainability. The framework consists of four components. First, a coupled mathematical model is developed for the integrated AEL-PRMD system, including the AEL and PRMD units with parallel and staged configurations, respectively (Fig. 9). The model predicts $NH_3$ removal, $H_2$ production, freshwater generation and internal energy recovery. Based on the process simulation results, a system-level energy analysis is performed to quantify electrical consumption, thermal demand, pumping requirements and electricity recovery, thereby determining the net energy consumption of the integrated process. TEA is subsequently conducted to evaluate wastewater treatment cost as the primary metric, together with levelised costs for freshwater, hydrogen and electricity as co-products. In parallel, LCA is carried out to quantify the environmental impacts of the integrated system under varying influent $NH_3$ concentrations and to identify the effect of process integration on environmental performance. Finally, the modelling, energy, economic and environmental results are interpreted collectively to evaluate trade-offs among treatment efficiency, resource recovery, energy consumption, economic feasibility and environmental sustainability.

Through this framework, the integrated AEL-PRMD system is assessed from both process and system perspectives, providing the basis for the detailed analyses presented in the following sections.

### Mathematical modelling of the integrated AEL-PRMD system

Figure 9 illustrates the system configuration of the AEL and PRMD modules within the integrated AEL-PRMD architecture, along with the key internal phenomena governing each system. The integrated AEL-PRMD system was modelled using coupled mass, energy and momentum balances for AEL and PRMD subsystems. In addition, auxiliary constitutive equations are accounted for, such as electrochemical reaction kinetics, gas-liquid mass transfer in the AEL and vapour permeation and temperature polarisation (TP) effects in the PRMD. Thermal and electrical coupling between the two units is incorporated through the heat-exchanger network and hydro-turbine. Detailed model equations for each individual unit are subsequently presented.

### Mathematical modelling of the AEL system

The mathematical model of AEL describes the electrochemical conversion of molecular $NH_3$ and the associated gas–liquid behaviour in the electrolyser. The $NH_3$ solution AEL shown in Fig. 9(a) is modelled as an isothermal steady-state CSTR based on the alkaline water electrolyser framework of Haug et al. [21], adapted for $NH_3$ electrolysis. Each cell consists of a zero-gap anode-separator-cathode configuration, and multiple cells may be arranged in cascade to achieve the target $NH_3$ removal efficiency. The governing electrode reactions are:

$$\text{Cathode}: 6H_2O + 6e^- \rightarrow 3H_2 + 6OH^- \quad (1)$$

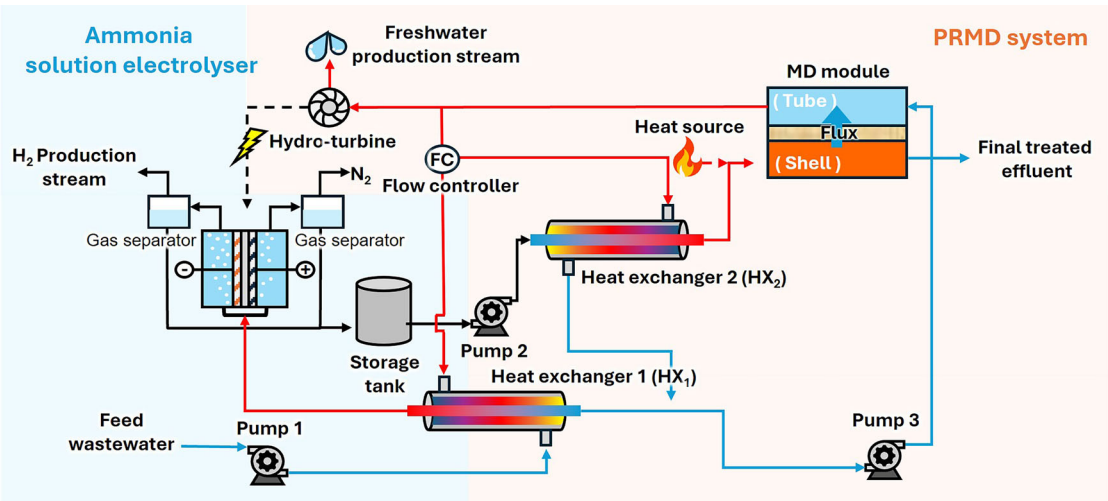



**Fig. 8 | The overall process schematic of the integrated AEL-PRMD system integrating the AEL and PRMD systems.** The system is mainly composed of an AEL and a PRMD system, together with heat exchangers, pumps, a storage tank, a heat source and a hydro-turbine. Feed wastewater passes through Pump 1 $HX_1$ before entering the AEL. The stream leaving the AEL is transferred to the PRMD system through the storage tank and Pump 2, then passes through $HX_2$ and the heat source before entering the MD module. The MD module separates the stream into the final treated effluent and freshwater production stream. The freshwater production stream is recovered after passing through the hydro-turbine, while permeate-side heat is recovered in $HX_1$ and $HX_2$ for feed preheating.

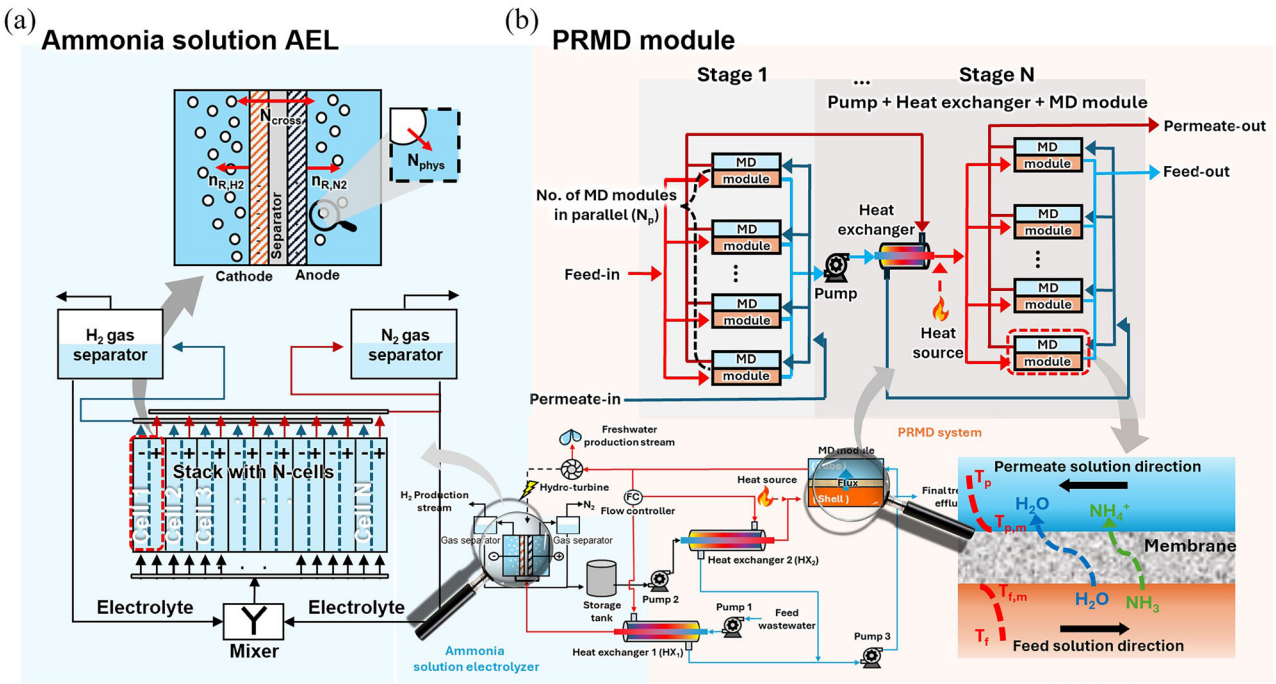



**Fig. 9 | Schematic diagram of the scaled-up integrated AEL-PRMD system with key transport and reaction phenomena in each unit. a** The scaled-up AEL is configured as a stack of multiple electrolysis cells with mixed electrolyte circulation. The electrolyte streams from the cathodic and anodic compartments are combined in the mixer and redistributed to the AEL stack. Each cell contains cathode and anode compartments separated by a separator, and the main reaction and transport terms considered in the cell are indicated, including gas generation, gas crossover through the separator and gas-liquid mass transfer. The gas-liquid outlet streams from the stack are directed to the $H_2$ and $N_2$ gas separators, where the gas products are separated from the electrolyte. **b** The PRMD system is arranged as a multi-stage module configuration from Stage 1 to Stage N. Each stage consists of a pump, heat exchanger, heat source and MD module, and multiple MD modules are connected in parallel within each stage. The enlarged MD module schematic indicates the feed and permeate solution directions, bulk temperatures, membrane surface temperatures, vapour and $NH_3$ transport across the membrane.

$$\text{Anode}: 2NH_3 + 6OH^- \rightarrow N_2 + 6H_2O + 6e^- \quad (2)$$

$$\text{Overall reaction}: 2NH_3 \rightarrow 3H_2 + N_2 \quad (3)$$

Steady state mass balances for the liquid and gas phases account for electrochemical reaction, gas desorption and species crossover through the separator[59,60]:

$$0 = \dot{V}_L^j\left(C_{in,i}^j - C_{out,i}^j\right) + N_{phys,i}^j \cdot A_{GL}^j \pm N_{cross,i} \cdot A_{sep} + \left(1 - f_{G,i}\right) \cdot \dot{n}_{R,i}^j \quad (4)$$

$$0 = \frac{\dot{V}_G^j}{R \cdot T}\left(p_{in,i}^j - p_{out,i}^j\right) - N_{phys,i}^j \cdot A_{GL}^j + f_{G,i} \cdot \dot{n}_{R,i}^j, \text{for j} = \text{ano, cat, i} = H_2, O_2 \quad (5)$$

where $\dot{V}_L$ and $\dot{V}_G$ represent the volumetric liquid flow rate and volumetric gas flow rate, respectively. $C_{in}$ is the inlet concentration, $A_{GL}$ the gas-liquid interfacial area, $A_{sep}$ the separator area, $\dot{n}_R$ the molar reaction flow rate, $R$ the gas constant, $T$ the operating temperature, $f_{G,i}$ the gas evolution efficiency of species $i$, defined as the fraction of the electrochemically generated species that is released directly as gas bubbles. $p_{in}$ and $p_{out}$ denote inlet partial pressure and outlet partial pressure of gas component $i$, respectively. $N_{phys}$ represents the desorption flux, that is, the mass transfer rate between the liquid electrolyte and the product gases[59], while $N_{cross}$ is the crossover flux through the separator[59], which are described by the following equations:

$$N_{phys,i}^j = k_{L,i}^j\left(C_i^{*,j} - C_{out,i}^j\right) \quad (6)$$

$$N_{cross,i} = \frac{D_i^{eff}}{d_{sep}}\left(C_{out,i}^{cat} - C_{out,i}^{ano}\right) \quad (7)$$

where $k$ is the species-specific mass transfer coefficient, $C_i^{*,j}$ the equilibrium concentration, $D_i^{eff}$ effective diffusion coefficient, $d_{sep}$ the separator thickness.

The reaction rates for each generated species follow Faraday's law:

$$\dot{n}_{R,i}^j = \frac{\nu_i^j \cdot J \cdot A_{ele}}{z \cdot F} \quad (8)$$

where $\nu_i$ denotes stoichiometric coefficient, $J$ the current density, $A_{ele}$ the area of the electrode, $z$ the charge transfer and $F$ the Faraday's constant.

The gas bubble pressure was calculated from the absolute pressure and Laplace pressure contribution[21,61]:

$$p^j = p^\circ + \Delta p^j \quad (9)$$

$$\Delta p^j = 4 \cdot \frac{\gamma}{d_b^j} \quad (10)$$

$$d_b^{cat} = 593.84 \times 10^{-6} \cdot (1 + 0.2 \cdot J)^{-0.25} \quad (11)$$

where $p^j$ is the gas bubble pressure at electrode $j$, $p^\circ$ the ambient pressure, $\Delta p^j$ the Laplace pressure contribution at electrode $j$, $\gamma$ the surface tension of the electrolyte, $d_b^j$ the gas bubble diameter at electrode $j$ and $d_b^{cat}$ the gas bubble diameter at the cathode.

The outlet mole fraction was obtained from the outlet gas partial pressure after accounting for the water vapour pressure:

$$p^j = \sum p^j_{out,i} + p_{H_2O} \tag{12}$$

$$y^j_{out,i} = \frac{p^j_{out,i}}{p^j - p_{H_2O}} \tag{13}$$

where $p_{H_2O}$ is the water vapour pressure and $y^j_{out,i}$ the outlet mole fraction of species $i$ at electrode $j$.

The gas evolution efficiency of $H_2$, defined as the fraction of electrochemically generated $H_2$ that is released directly as gas bubbles, was calculated as a function of current density[62]:

$$f_{G,H_2} = 0.5653 \cdot \left(1 - \exp(-0.002061 \cdot J)\right) \tag{14}$$

The gas bubble volume, bubble surface area and gas holdup volume, which are later used to obtain the gas-liquid interfacial area, were calculated using the following relations[61,63]:

$$V^j_b = \frac{\pi}{6} \cdot \left(d^j_b\right)^3 \tag{15}$$

$$S^j_b = \pi \cdot \left(d^j_b\right)^2 \tag{16}$$

$$V^j_{gas} = \varepsilon^j \cdot V_{hcell} \cdot \frac{p^\circ}{p^j} \tag{17}$$

$$\varepsilon^j = \frac{V_{gas}}{V_{total}} \tag{18}$$

where $V^j_b$ is the volume of a single gas bubble at electrode $j$, $S^j_b$ the surface area of a single gas bubble at electrode $j$, $V^j_{gas}$ the gas volume at electrode $j$, $\varepsilon^j$ the gas holdup fraction at electrode $j$, $V_{hcell}$ the half-cell volume, $V_{gas}$ the total gas volume and $V_{total}$ is the total volume of gas and liquid. The gas-liquid interfacial area was then calculated from the gas volume and bubble diameter:

$$A^j_{GL} = \frac{V^j_{gas}}{V^j_b} S^j_b = 6 \cdot \frac{V^j_{gas}}{d^j_b} \tag{19}$$

To calculate the electrical energy consumption of the AEL, the cell voltage was determined by accounting for the open-circuit voltage, activation overpotential and ohmic overvoltage. The open-circuit voltage was calculated from the reversible voltage, temperature correction and gas partial-pressure contribution[20,64].

$$V_{oc} = V^0_{rev} + \left(T - T_{ref}\right) \times \frac{S^\circ}{zF} + 2.3 \times \frac{RT}{zF} \log\left(\frac{\left(p^{cat}\right)^3 \cdot \frac{p^{ano}}{(p^\circ)^4}}{\alpha^2_{NH_3}}\right) \tag{20}$$

$$\log\left(\alpha_{H_2O+KOH}\right) = -0.02255 \cdot m_{KOH} + 0.001434 \cdot m^2_{KOH} + \frac{1.38 \cdot m_{KOH} - 0.9254 \cdot m^2_{KOH}}{T} \tag{21}$$

where $V_{oc}$ is the open-circuit voltage, $V^0_{rev}$ the reversible potential at standard conditions, $T_{ref}$ the reference temperature, $S^\circ$ the entropy change, $p^{cat}$ and $p^{ano}$ are the gas pressures at the cathode and anode, respectively. $\alpha^2_{NH_3}$ tis he ammonia activity, $\alpha_{H_2O+KOH}$ is the activity term for the $H_2O$-KOH electrolyte system and $m_{KOH}$ is the molality of KOH.

The activation overpotential includes the effect of bubble coverage on the electrode surface, whereas the ohmic overvoltage accounts for the resistive losses associated with the electrodes, electrolyte and separator. It was calculated using the anodic and cathodic kinetic contributions[20,65]:

$$V_{act} = \frac{RT}{zF\alpha^{ano}} \ln\left(\frac{J}{J^{ano}_0(1-\theta)}\right) + \frac{RT}{zF\alpha^{cat}} \ln\left(\frac{J}{J^{cat}_0(1-\theta)}\right) \tag{22}$$

$$J^j_0 = r^j_M \exp\left(-\frac{\triangle G^j_C}{R}\left(\frac{1}{T} - \frac{1}{T_{ref}}\right)\right) \cdot J^j_{0,ref} \tag{23}$$

where $V_{act}$ is the activation overpotential, $\alpha^{ano}$ and $\alpha^{cat}$ the charge transfer coefficients for the anode and cathode, respectively. $J^{ano}_0$ and $J^{cat}_0$ are the exchange current densities for the anode and cathode, respectively and $\theta$ is the fractional bubble coverage. $J^j_0$ is the exchange current density at electrode $j$ and $J^j_{0,ref}$ is the reference exchange current density at electrode $j$. $r^j_M$ is the roughness factor of electrode $j$, and $\Delta G^j_C$ is the Gibbs free energy of activation at electrode $j$.

The fractional bubble coverage was estimated as a function of temperature, current density, limiting current density and water vapour pressure[66]:

$$\theta = \left(-97.25 + 182\frac{T}{T_{ref}} - 84\left(\frac{T}{T_{ref}}\right)^2\right) \cdot \left(\frac{J}{J_{\lim}}\right)^{0.3} \cdot \frac{p^\circ}{p^\circ - p_{H_2O}} \tag{24}$$

where $J_{\lim}$ is the limiting current density at full bubble coverage.

The ohmic overvoltage was calculated from the combined electrode, electrolyte and separator resistances:

$$V_{ohm} = J \cdot \left(R_{ele} + R_{ely} + R_{sep}\right) \tag{25}$$

where $V_{ohm}$ is the ohmic overvoltage, $R_{ele}$ the electrode resistance, $R_{ely}$ the electrolyte resistance and $R_{sep}$ the separator resistance.

The electrode resistance was calculated from the effective resistivity and electrode thickness[67]:

$$R_{ele} = \rho^{ano}_{eff} \cdot \left(\frac{\delta^{ano}}{A_{ele}}\right) + \rho^{cat}_{eff} \cdot \left(\frac{\delta^{cat}}{A_{ele}}\right) \tag{26}$$

$$\rho^j_{eff} = \frac{\rho^j_0}{\left(1 - \varepsilon_{ele}\right)^{\frac{3}{2}}} \tag{27}$$

where $\rho^j_{eff}$ is the effective resistivity of the electrode $j$, $\delta^j$ the thickness of the electrode $j$, $\rho^j_0$ the dense electrode resistivity at the reference temperature and $\varepsilon_{ele}$ the electrode porosity.

The electrolyte resistance was calculated by accounting for the electrolyte conductivity and bubble coverage effect[65]:

$$R_{ely} = \frac{1}{\sigma_{ely}} \cdot \left(\frac{d^{as}}{A_{ele}} + \frac{d^{cs}}{A_{ele}}\right) + \frac{1}{\sigma_{ely}} \cdot \left(\frac{d^{as}}{A_{ele}} + \frac{d^{cs}}{A_{ele}}\right) \cdot \left(\frac{1}{\left(1 - \frac{2}{3}\theta\right)^{\frac{3}{2}}} - 1\right) \tag{28}$$

where $\sigma_{ely}$ is the ionic conductivity of the electrolyte, $d^{as}$ the distance between the anode and the separator and $d^{cs}$ the distance between the cathode and the separator. The ionic conductivity of the KOH electrolyte was calculated as a function of KOH weight fraction and temperature[68]:

$$\begin{aligned}\sigma_{ely}\left(w_{KOH}, T\right) = {} & 2.96396 - 0.02371T - 0.112269w_{KOH} \\ & + 5.7 \times 10^{-5}T^2 + 0.00173{w_{KOH}}^2 + 4.7 \times 10^{-4}w_{KOH} \\ & - 3.6 \times 10^{-8}T^3 + 2.7 \times 10^{-6}{w_{KOH}}^3 \\ & - 8.9 \times 10^{-6}T \cdot {w_{KOH}}^2 + 2.4 \times 10^{-7} \times T^2 \cdot w_{KOH}\end{aligned} \tag{29}$$

where $\sigma_{ely}$ is the ionic conductivity of the KOH electrolyte, $w_{KOH}$ is the weight fraction of KOH and $T$ is the operating temperature. This correlation is valid for 273.15 K ≤ $T$ ≤ 373.15 K and 10% ≤ $w_{KOH}$ ≤ 45%.

The separator resistance was calculated from the separator thickness, porosity, tortuosity and conductivity[69]:

$$R_{sep} = \frac{\tau_{sep}^2 \delta_{sep}}{\sigma_{sep} \omega_{sep} \varepsilon_{sep} A_{sep}} \tag{30}$$

$$\sigma_{sep} = 10^3 - 5.25 \cdot T + 7 \cdot 10^{-3} \cdot T^2 \tag{31}$$

where $\tau_{sep}^2$ is the separator tortuosity, $\delta_{sep}$ is the separator thickness, $\sigma_{sep}$ is the separator conductivity, $\omega_{sep}$ is the separator wettability factor, $\varepsilon_{sep}$ is the separator porosity and $A_{sep}$ is the separator area.

Incorporating all key variables presented above, the following boundary conditions for the inlet concentrations and gas partial pressures are applied to Eqs. (4)-(5):

$$C_{in,i}^{ano} = C_{in,i}^{cat} = C_i^{mix} \tag{32}$$

$$C_i^{mix} = \frac{C_{out,i}^{ano} + C_{out,i}^{cat}}{2} \tag{33}$$

$$p_{in,i}^{ano} = p_{in,i}^{cat} = 0 \tag{34}$$

where $C_i^{mix}$ is the mixed electrolyte concentration of species $i$.

### Mathematical modelling of the PRMD system

The mathematical model of the PRMD subsystem is developed based on direct contact membrane distillation (DCMD), with the additional feature that pressure is applied on the permeate side. For scale-up, parallel and multi-stage module configurations are adopted, as illustrated in Fig. 9(b). Within each MD module, a hot feed stream and a cold permeate stream flow counter currently, which are separated by hydrophobic, porous hollow-fibre membranes.

Mass, energy and momentum balances along the module length are expressed as[13]:

$$\frac{dF_i^c}{dz} = \mp J_i \left( N_{fiber} \pi d_{lm} \right) \text{ for } c = \text{F, P, } i = \text{ w, a} \tag{35}$$

$$\frac{d\left[ \left( F_w^c C_{p,w} + F_a^c C_{p,\text{a}} \right) T_b^c \right]}{dz} = \mp Q^c \tag{36}$$

$$\frac{dP^c}{dz} = \mp \frac{32 \mu^c}{d_h^2} v^c \tag{37}$$

where the superscript $c$ denotes the feed (F) or permeate (P) channel side, with the negative and positive signs in Eqs. (35)–(37) corresponding to the feed and permeate channels, respectively. The subscripts $w$ and $a$ denote the water and ammonia, respectively. $F$ is the mass flow rate, $N_{fiber}$ the number of membrane fibres, $d_{lm}$ logarithmic mean diameter, $C_p$ the specific heat capacity, $Q$ the heat flux, $\mu$ the viscosity, $v$ the linear velocity and $d_h$ hydraulic diameter.

In the aqueous solution within the AEL-PRMD system, ammonia exists as $NH_3$ and $NH_4^+$. Electrochemical reactions in the AEL and vapour transport in the MD module involve molecular $NH_3$; therefore, its concentration is required. The molecular $NH_3$ concentration is calculated as[70]:

$$C_a = \frac{C_{TAN}}{1 + 10^F} \tag{38}$$

$$F = 4 \times 10^{-8} T^3 + 9 \times 10^{-5} T^2 - 0.0356T + 10.072 - pH \tag{39}$$

where $C_{TAN}$ is the concentration of total $NH_3$ in any form, the exponent factor $F$, which is a function of temperature and pH of the aqueous solution[71]. The correlation is valid for 0–100 °C and pH 7.5–11.5[72].

The linear velocities on the feed and permeate sides are defined as follows:

$$v^F = \frac{F^F}{\rho^F \left( \frac{\pi d_{sh}^2}{4} - \frac{N_{fiber} \pi d_o^2}{4} \right)} \tag{40}$$

$$v^P = \frac{F^P}{\rho_w \left( \frac{N_{fiber} \pi d_i^2}{4} \right)} \tag{41}$$

where $d_{sh}$ is the shell side diameter, $d_o$ and $d_i$ are the outer and inner diameters of the hollow fibre, respectively.

The transmembrane vapour flux of component i was calculated from the membrane resistance and the vapour pressure difference between the feed and permeate membrane surfaces[12]:

$$J_i = \frac{1}{R_{i,m}} \left( P_{i,m}^F - P_{i,m}^P \right) \tag{42}$$

where the subscript $i$ denotes water and $NH_3$, $P_m$ is the vapour pressure at the surface of the membrane. The membrane resistance $R_m$ is defined as:

$$R_m = \frac{\tau_m \delta_m}{\varepsilon_m} \frac{RT}{M_w} \left( \frac{1}{D_W^k} + \frac{p_a}{P D_{wa}^o} \right) \tag{43}$$

$$D_W^k = \frac{2r}{3} \sqrt{\frac{8RT}{\pi M_w}} \tag{44}$$

where $\tau_m$ is the membrane tortuosity, $\delta_m$ the membrane thickness and $\varepsilon_m$ the membrane porosity, $M_w$ the molecular weight of water, $D_W^k$ the Knudsen diffusion coefficient of water vapour, $p_a$ the partial pressure of air trapped in the membrane pores, $P$ the total pressure and $D_{wa}^o$ the molecular diffusion coefficient of water vapour in air and $r$ the membrane pore radius.

The water vapour pressure at the membrane surface was calculated from the water mole fraction and saturation vapour pressure:

$$P_w = x_w \cdot P_w^* \tag{45}$$

where $P_w$ is the water vapour pressure at the membrane surface, $x_w$ is the water mole fraction and $P_w^*$ is the saturation vapour pressure of pure water. The partial pressure of $NH_3$ was calculated from the molecular $NH_3$ concentration and Henry's law constant.

$$P_m = C_a / H_a \tag{46}$$

$$H_a = H_{a,ref} \times \exp\left( 4200 \left( \frac{1}{T} - \frac{1}{T_{ref}} \right) \right) \tag{47}$$

where $P_m$ is the partial pressure of $NH_3$ at the membrane surface, $C_a$ the molecular $NH_3$ concentration in the aqueous solution, $H_a$ Henry's law constant for $NH_3$ and $H_{a,ref}$ the Henry's law constant at the reference temperature.

Heat transfer in the MD module is described using boundary-layer resistance at the membrane surfaces and membrane-internal resistance associated with conduction and latent heat transfer. The heat transfer coefficient on the tube side is calculated using the following empirical

correlations, depending on the Reynolds number[73,74]:

$$Nu^F = \frac{h^F d_i}{k^F} = 1.62\left(Re^F \times Pr^F \times \frac{d_i}{L}\right)^{0.33} \text{ for } Re^F < 2100 \quad (48)$$

$$Nu^F = \frac{h^F d_i}{k^F} = 0.023\left(Re^F\right)^{0.8}\left(Pr^F\right)^{0.3} \text{for } 2100 < Re^F < 6000 \quad (49)$$

$$Nu^F = \frac{h^F d_i}{k^F} = 0.027\left(Re^F\right)^{0.8}\left(Pr^F\right)^{0.33} \text{for } Re^F > 6000 \quad (50)$$

where $Nu$ is the Nusselt number, $h$ is the heat transfer coefficient and $k$ is the thermal conductivity of the solution. $Re$ and $Pr$ are the Reynolds and Prandtl numbers, respectively, and $L$ is the hollow-fibre length. For the shell side, the heat transfer coefficient was calculated using the shell-side Nusselt number correlation:

$$Nu^P = \frac{h^P d_h}{k^P} = 0.206\left(Re^P \times \cos\theta_y\right)^{0.63}\left(Pr^P\right)^{0.36} \quad (51)$$

where $\phi$ is the packing density $\theta_y$ is the yaw angle determined by module flow configuration, with 0 ° for cross flow, 90 ° for parallel flow, 87° for a shell-and-tube capillary membrane module. The hydraulic diameter was calculated from the packing density and outer diameter of the hollow fibre:

$$d_h = \frac{1-\phi}{\phi} d_o \quad (52)$$

where $d_h$ is the hydraulic diameter.

The heat transfer rate from the bulk solution to the membrane surface on both feed and permeate sides is given by[75]:

$$Q^F = h^F N_{fiber} \pi d_o \left(T_b^F - T_m^F\right) \quad (53)$$

$$Q^P = h^P N_{fiber} \pi d_i \left(T_m^P - T_b^P\right) \quad (54)$$

where the subscripts $b$ and $m$ denote bulk and membrane surface, respectively. At steady state, heat flux continuity is imposed across the boundary layers and membrane:

$$Q^F = Q^P = Q^M \quad (55)$$

$$Q^M = N_{fiber} \pi d_{lm}\left[\sum\nolimits_i J_i \Delta H_i + \frac{k_m}{\delta_m}\left(T_m^F - T_m^P\right)\right] \quad (56)$$

where the superscript $M$ denotes the membrane, $\Delta H$ the enthalpy of vapourisation, $k_m$ the conductive heat transfer coefficient for a two-phase composite material and $\delta_m$ the membrane thickness. These equations account for temperature polarisation and pressure-dependent vapour transport. The effective thermal conductivity of the membrane was calculated as a porosity-weighted contribution of the gas and polymer phases:

$$k_m = \varepsilon_m k_g + \left(1-\varepsilon_m\right) k_p \quad (57)$$

where $k_m$ is the effective thermal conductivity of the membrane, $k_g$ the thermal conductivity of the gas phase and $k_p$ the thermal conductivity of the polymer phase. The logarithmic mean diameter of the hollow-fibre membrane was calculated from the inner and outer diameters:

$$d_{lm} = \frac{d_o - d_i}{\ln\left(\frac{d_o}{d_i}\right)} \quad (58)$$

where $d_{lm}$ is the logarithmic mean diameter of the hollow-fibre membrane.

Permeate-side pressurisation is applied in the PRMD system to operate the hydro-turbine (HT) and recover freshwater, but membrane wetting may occur if the liquid-entry pressure (LEP) is exceeded. The LEP is determined by membrane pore size, surface tension and contact angle using the Young-Laplace equation:

$$LEP = -\frac{2\Theta\sigma\cos\theta}{r_{pore}} \quad (59)$$

where $\Theta$ is the geometric factor related to the pore structure, $\sigma$ is the interfacial tension, $\theta$ is the liquid-solid contact angle, $r_{pore}$ is the radius of membrane pores. To prevent membrane wetting and structural deformation, the LEP was used to define the maximum allowable operating pressure. The permeate-side pressure was limited to 10 bar, and when the calculated LEP exceeded this value, the operating pressure was capped at 10 bar. This limit follows experimental observations that membrane structural transitions occur above approximately 10 bar[16].

### Calculation of energy requirements in the integrated AEL-PRMD system

To evaluate the overall energy performance of the integrated AEL-PRMD process, total energy is defined as:

$$E_{tot} = E_{ele} + E_{pump} + E_{heat} - E_{gen} \quad (60)$$

where $E_{ele}$ is the electrical energy consumed by the AEL, $E_{pump}$ the pumping energy required to compensate for pressure losses, $E_{heat}$ the thermal energy supplied by external heat sources and $E_{gen}$ the electricity generated by the HT. The individual terms in Eq. (60) were calculated as described below:

The AEL electricity consumption is calculated from the total cell voltage of the stack:

$$E_{ele} = V_{cell} \cdot N_{cell} \cdot J \cdot \frac{A_{AEL}}{\eta_{AEL}} \quad (61)$$

where $V_{cell}$ is the total overpotential of the cell, $N_{cell}$ the number of cells, $A_{AEL}$ the electrode area and $\eta_{AEL}$ the efficiency of AEL.

The total pumping energy includes the wastewater feed pump, HX-associated pressure recovery pumps and permeate-side pressurisation pumps. The general expression for pumping power is:

$$E_{pump} = \frac{1}{\eta_{pump}} \frac{F_l\left(P_{out,l} - P_{in,l}\right)}{\rho_l} \quad (62)$$

where $\eta_{pump}$ is the efficiency of the pump and the subscript $l$ denotes each pressure boosting zone. $F_l$ is the mass flow rate through the pump and $P_{in,l}$ and $P_{out,l}$ correspond to the pressures at the inlet and outlet of the respective segment.

The heat transfer rate in each heat exchanger was calculated as follows:

$$q_{req}^C = F^C C_p\left(T_{target} - T_{in}^C\right) \quad (63)$$

$$q_{max}^H = F^H C_p\left(T_{in}^H - \left(T_{in}^C + \Delta T_{min}\right)\right) \quad (64)$$

$$Q = \eta_{HX} \times \min\left(q_{req}^C, q_{max}^H\right) \quad (65)$$

$$T_{out}^C = T_{in}^C + \frac{Q}{F^C C_p^C} \quad (66)$$

$$T_{out}^H = T_{in}^H - \frac{Q}{F^H C_p^H} \quad (67)$$

where $q_{req}^{C}$ is the heat required on the cold side to reach the target temperature, $q_{\max}^{H}$ is the hot side maximum available heat, $C_p$ is the mass specific heat capacity, $Q$ is the actual heat transfer in the HX, $\Delta T_{\min}$ is the minimum approach temperature, $\eta_{HX}$ is the efficiency of HX, $T_{out}$ is the outlet temperature. The superscripts $H$ and $C$ the hot and cold sides of the HX, respectively.

The equivalent electrical energy of the supplementary heat supplied to the PRMD system was calculated as follows[46,47,76,77]:

$$E_{heat} = \frac{\Delta H_v \cdot \eta_{turbine} \cdot V_{H_2O}}{GOR} \tag{68}$$

where $E_{heat}$ is the equivalent electrical energy of the thermal energy, $\Delta H_v$ the specific enthalpy drop obtainable from a notional steam expansion, $V_{H_2O}$ the volumetric flow rate of produced water and $\eta_{turbine}$ the efficiency of the turbine. The gained output ratio (GOR), which reflects the efficiency of the thermal desalination system, can be calculated using:

$$GOR = \frac{H_{vap} V_{H_2O}}{Q_{net}} \tag{69}$$

where $H_{vap}$ is the latent heat of vaporisation of the solution, $Q_{net}$ is the additional heat rate of the total process.

Finally, electricity generation $E_{gen}$ through the HT is calculated as:

$$E_{gen} = \eta_{HT}\left(P_{in}^{HT} - P_{env}\right)\frac{\left(F_{out}^{P} - F_{in}^{P}\right)}{\rho^{P}} \tag{70}$$

where $\eta_{HT}$ represents the efficiency of the HT, $P_{in}^{HT}$ the inlet pressure of the HT and $P_{env}$ the environmental pressure and $\left(F_{out}^{P} - F_{in}^{P}\right)$ correspond to the net mass flow rate passing through the HT.

## Simulation conditions and numerical procedure

The simulation analyses presented in the following sections were performed under the baseline operating conditions and module specifications summarised in Table 6. The influent $NH_3$ concentration was selected to represent typical conditions for semiconductor wastewater[78,79]. System capacity was scaled by increasing the number of AEL cells, while maintaining the operating conditions within recommended ranges reported in the literature[21,80]. The thermophysical properties of the feed solution and the model parameters used in the integrated AEL-PRMD system are provided in Tables 7 and 8, respectively.

**Table 6 | Baseline operating conditions and module specifications**

| | Description (*Symbol*) | Value [unit] |
|---|---|---|
| Feed conditions | Wastewater temp. ($T_f$) | 25 [°C] |
| | Wastewater flow rate ($V_f$) | 12 [m³/day] |
| | Wastewater $NH_3$ conc. ($C_f$) | 100 [ppm] |
| | Wastewater pH | 12 [-] |
| MD operating conditions | Hot feed temp. ($T_{h,f}$) | 90 [°C] |
| | Hot feed pressure ($P_{h,f}$) | 1.5 [bar] |
| | Waste heat temp. ($T_{WT}$) | 95 [°C] |
| | pH | 7 [-] |
| AEL operating conditions | Operating temp. ($T_{ele}$) | 25, 45, 65 [°C] |
| | Current density ($J_{ele}$) | 0.15 [A/cm²] |
| AEL module specifications | Half-cell volume ($V_{cell}$) | $3.48 \times 10^{-4}$ [m³] |
| | Electrode area of each cell ($A_{ele}$) | $1.50 \times 10^{-2}$ [m²] |
| | Electrode thickness ($\delta_{ele}$) | $2.0 \times 10^{-3}$ [m] |
| | Separator area ($A_{sep}$) | $2.32 \times 10^{-2}$ [m²] |
| | Number of cells ($N_{cell}$) | 10 [-] |
| | AEL efficiency ($\eta_{ele}$) | 0.70 [-] |
| MD module specifications | Total membrane area ($A$) | 20.6 [m²] |
| | Membrane thickness ($\delta$) | 60 [$\mu$m] |
| | Membrane contact angle ($\theta$) | 130 [°] |
| | Number of fibres ($N_{fiber}$) | 36,848 [-] |
| | Number of parallel modules ($N_p$) | 6 [-] |
| | Number of stages ($N_s$) | 2 [-] |

**Table 7 | Temperature-dependent thermophysical properties of $NH_3$ solution used in the AEL model**

| |
|---|
| **Density of $NH_3$ solution, $\rho$ [kg/m³]** |
| $\rho(T) = -4.82\times10^{-7}T^4 + 5.22\times10^{-4}T^3 - 0.21T^2 + 36.84T - 1571.94$[105] |
| **Heat capacity, $C_p$ [J/kg/K]** |
| $C_p(T) = -5.71\times10^{-6}T^4 + 1.31\times10^{-2}T^3 - 7.59T^2 + 1762.32T - 71721.49$[106] |
| **Viscosity, $\mu$ [Pa·s]** |
| $\mu(T) = 1.49\times10^{-12}T^4 - 1.81\times10^{-9}T^3 + 8.32\times10^{-7}T^2 - 1.72\times10^{-4}T + 0.013$[107] |
| **Latent heat,$H$ [J/kg]** |
| $H(T) = -3.77\times10^{7} + 1.03\times10^{6}T^1 - 6.08\times10^{3}T^2 + 1.54\times10T^3 - 1.49\times10^{-2}T^4$[108] |

**Table 8 | Electrochemical and transport parameters used in the AEL model**

| Description | Symbol | Value [unit] | Ref. |
|---|---|---|---|
| Mass transfer coefficient of $H_2$ in the anode | $k_{L,H_2}^{ano}$ | $4.2\times10^{-4}$ [m/s] | 59 |
| Mass transfer coefficient of $H_2$ in the cathode | $k_{L,H_2}^{cat}$ | $3.3\times10^{-4}$ [m/s] | 59 |
| Mass transfer coefficient of $N_2$ in the anode | $k_{L,N_2}^{ano}$ | $2.6\times10^{-4}$ [m/s] | 59 |
| Mass transfer coefficient of $N_2$ in the cathode | $k_{L,N_2}^{cat}$ | $2.1\times10^{-4}$ [m/s] | 59 |
| Binary diffusion coefficient of $H_2$ | $D_{H_2}$ | $5.6\times10^{-9}$ [m²/s] | 109 |
| Binary diffusion coefficient of $N_2$ | $D_{N_2}$ | $3.5\times10^{-9}$ [m²/s] | 110 |
| Porosity of the separator | $\varepsilon_s$ | 0.50 [-] | 110 |
| Tortuosity of the separator | $\tau_s$ | 3.14 [-] | 111 |
| Surface tension of electrolyte | $\gamma$ | 0.083 [N/m] | 112 |
| Gas bubble diameter in the anode | $d_b^{ano}$ | $2.1\times10^{-4}$ [m] | 59 |
| Reversible potential at standard conditions | $V_{rev}^{0}$ | 0.059 [V] | 40 |
| Cathode roughness factor | $r_M^{cat}$ | 1.05 [-] | 113 |
| Anode roughness factor | $r_M^{ano}$ | 1.25 [-] | 113 |
| Free energy of activation of the cathode | $\Delta G_C^{cat}$ | 26.6 [kJ/mol] | 113 |
| Free energy of activation of the anode | $\Delta G_C^{ano}$ | 32.6 [kJ/mol] | 113,114 |
| Limiting current density at 100% bubble coverage | $J_{\lim}$ | 30 [A/cm²] | 69 |
| Resistivity of the dense electrode at ref. temperature | $\rho_0^j$ | $6.4\times10^{-6}$ [Ω·cm] | 69 |
| Porosity of the electrode | $\varepsilon_{ele}$ | 0.30 [-] | 115 |
| Distances between the electrode and the separator | $d^{js}$ | $9.0\times10^{-4}$ [m] | 115 |
| Separator thickness | $\delta_s$ | $5.0\times10^{-4}$ [m] | 115 |
| Wettability factor | $\omega_s$ | 0.85 [-] | 21 |

**Table 9 | Operating current density ($J_{ele}$) [A/cm$^2$] at a fixed AEL temperature ($T_{ele}$) of 65 °C as a function of wastewater $NH_3$ concentration ($C_f$) and target $NH_3$ removal efficiency ($\eta_{NH3,rem}$)**

| $C_f$ \ $\eta_{NH3,rem}$ | 99.5% | 95% | 90% | Total electrode area [m$^2$] |
|---|---|---|---|---|
| 5 ppm | $7.8 \times 10^{-4}$ | $7.47 \times 10^{-4}$ | $7.1 \times 10^{-4}$ | 0.15 |
| 50 ppm | 0.078 | 0.0747 | 0.0708 | 0.15 |
| 500 ppm | 0.4/0.38 | 0.4/0.3475 | 0.4/0.3081 | 0.3 |
| 1000 ppm | 0.4/0.4/ 0.4/0.36 | 0.4/0.4/ 0.4/0.295 | 0.4/0.4/ 0.4/0.216 | 0.6 |

The operating current densities and total electrode areas specified for different wastewater $NH_3$ concentrations and target $NH_3$ removal efficiencies were used in the subsequent performance analyses and are summarised in Table 9. The AEL was assumed to operate at a maximum current density of 0.4 A/cm$^2$, which lies within the recommended operating range for AWE systems[79]. To achieve the desired $NH_3$ removal efficiencies under different influent concentrations while respecting this limit, a cascade electrolyser configuration was adopted.

To solve the heat-integrated AEL-PRMD system consistently, an iterative calculation scheme was applied to account for the thermal coupling between the AEL and PRMD units through $HX_1$ and $HX_2$. As shown in Fig. 10, the split-stream flow rate to the heat exchangers was first guessed and then updated using the MD permeate outlet conditions until a consistent heat-exchanger flow allocation was obtained. The iterative procedure continued until the difference in the split-stream variables between successive iterations was less than $1 \times 10^{-3}$. The system of ordinary differential and algebraic equations for the MD module was solved using the "MATLAB ode45 solver", following the algorithm reported in the literature[12].

## Cost model

A levelised-cost framework was adopted to evaluate the economic feasibility of the integrated AEL-PRMD system. Because wastewater treatment is the primary system function, while freshwater, hydrogen and electricity are co-products, the analysis includes both a unit wastewater treatment cost and levelised cost metrics for each recovered product.

The capital recovery factor (*CRF*) converts the total capital investment into an equivalent annualised cost:

$$CRF = \frac{i \times (i+1)^n}{(i+1)^n - 1} \tag{71}$$

where $i$ is the annual discount rate and $n$ the project lifetime.

The annual salvage value (*ASV*) is calculated using the sinking fund factor (*SFF*):

$$ASV = SFF \times LC_{\text{inv}} \tag{72}$$

$$SFF = \frac{i}{(i+1)^n - 1} \tag{73}$$

Annual electricity consumption is calculated from the total system power demand:

$$E_{con}^{yr} = 365 \times (W_{\text{p}} + W_{ele}) \times t_{\text{op}} \tag{74}$$

where $E_{con}^{yr}$ is the annual total electricity consumption, $W_p$ the total pump power demand, $W_{ele}$ the electrolyser power demand and $t_{op}$ the daily operating time.

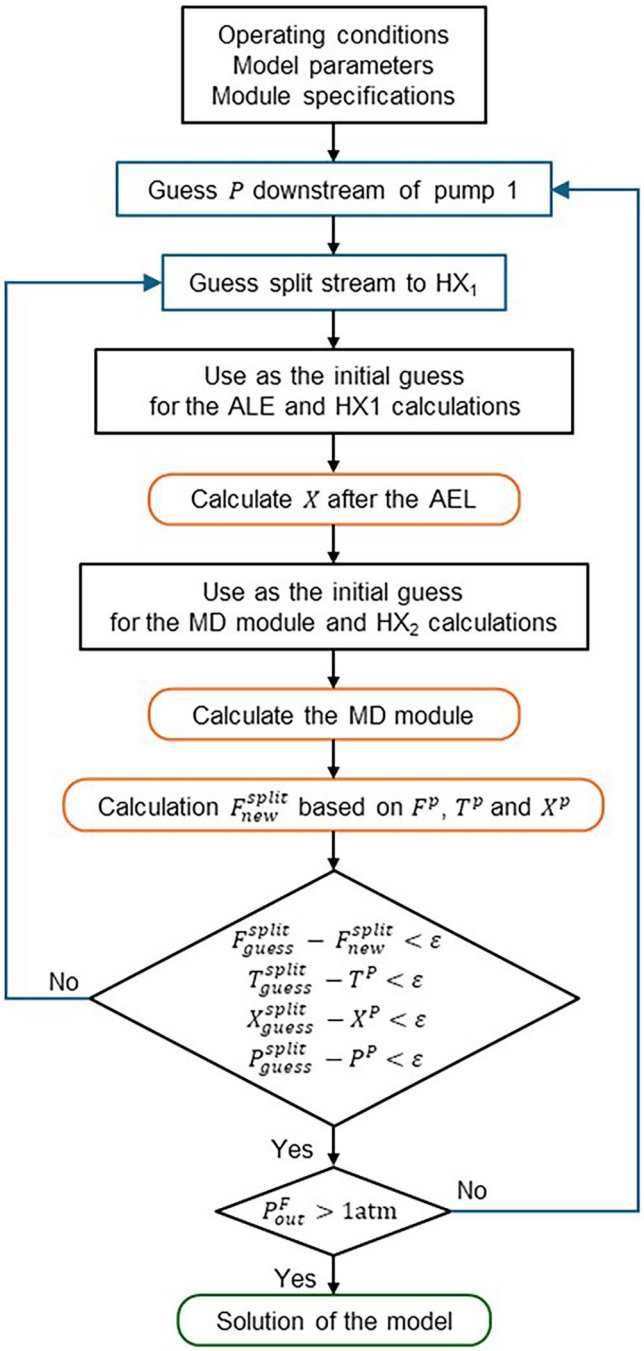



**Fig. 10 | Flowchart for the simulation procedure of the integrated AEL-PRMD system.** This flowchart shows the overall calculation algorithm, including input specification, AEL and PRMD module calculations, HX split-stream flow rate update and convergence check. Thermal coupling through $HX_1$ and $HX_2$ is handled iteratively, and the final system performance indicators are then obtained.

Electricity-related costs or credits are incorporated through annual electricity demand:

$$ARC_{LCOW} = (-E_{net}^{yr}) \times C_E \tag{75}$$

$$ARC_{LCOE} = E_{con}^{yr} \times C_E \tag{76}$$

$$ARC_{LCOH} = E_{ele}^{yr} \times C_E \tag{77}$$

where $ARC_{LCOW}$ is the annual running cost term used in the LCOW formulation, $ARC_{LCOE}$ the annual running cost term used in the LCOE formulation, $ARC_{LCOH}$ the annual running cost term used in the LCOH formulation, $-E_{net}^{yr}$ the annual net grid electricity demand, $C_E$ the unit electricity price $E_{con}^{yr}$ the annual total electricity consumption of the integrated system and $E_{ele}^{yr}$ the annual electricity consumption of the electrolyser.

The negative sign in Eq. (75) indicates that internally recovered electricity from the PRMD subsystem offsets external electricity purchases. In this way, the LCOE and LCOH formulations reflect the electricity burden associated with producing each output, while LCOW reflects the benefit of internal electricity recovery through a net electricity offset term.

Energy performance of the integrated AEL-PRMD system is evaluated using the following indicators:

$$SEC = \frac{E_{con}^{yr}}{V_w} \tag{78}$$

$$SEG = \frac{E_{gen}^{yr}}{V_w} \tag{79}$$

$$SNE = SEG - SEC \tag{80}$$

where SEC is the specific electricity consumption, SEG the specific electricity generation, SNE the specific net energy, $E_{gen}^{yr}$ the annual electricity generation of the integrated system and $V_w$ the annual freshwater production.

The total annualised net system cost, $C_{ann}$, is defined as:

$$C_{ann} = LC_{inv} \times CRF + LC_{O\&M} - ASV + ARC \tag{81}$$

where $LC_{inv}$ is the capital investment cost, $CRF$ the capital recovery factor and $LC_{O\&M}$ the annual operation and maintenance cost. The final term accounts for the generated electricity in the integrated system that partially offsets external electricity demand.

The treatment-oriented cost metric, namely the unit wastewater treatment cost, is defined as:

$$C_{ww} = \frac{C_{ann}}{V_{ww}} \tag{82}$$

where $C_{ww}$ is the unit wastewater treatment cost and $V_{ww}$ the annual volume of treated wastewater. This metric is used to compare the integrated AEL-PRMD system with conventional wastewater treatment technologies.

The economic performance of the co-products is evaluated using the levelised costs of water (LCOW), electricity (LCOE) and hydrogen (LCOH), defined as:

$$\mathrm{LCOW} = \frac{LC_{inv} \times CRF + LC_{o\&M} + ARC_{LCOW} - ASV}{V_w} \tag{83}$$

$$\mathrm{LCOE} = \frac{LC_{inv} \times CRF + LC_{o\&M} + ARC_{LCOE} - ASV}{E_{gen}^{yr}} \tag{84}$$

$$\mathrm{LCOH} = \frac{LC_{inv} \times CRF + LC_{o\&M} + ARC_{LCOH} - ASV}{H_{2_{gen}}} \tag{85}$$

where $H_{2_{gen}}$ is the annual hydrogen production.

The cost parameters and literature-based assumptions used in the analysis are listed in Table 10.

**Table 10 | Cost parameters for the integrated AEL-PRMD module**

| Description | *Symbol* | Ref | Value [unit] |
|---|---|---|---|
| AWE stack cost | - | 116 | 340 [$/kWh] |
| Balance of plants | BOP | 116 | 55% of AWE [-] |
| Labor cost | - | 117 | 0.3% of CAPEX [-] |
| Capital recovery factor | *CRF* | | 0.08 [-] |
| Sinking fund factor | *SFF* | | 0.03 [-] |
| Operating year of the plant | *n* | 116 | 20 [yr] |
| Annual discount rate | *i* | 118 | 5 [%] |
| Unit electricity price | $C_E$ | 119 | 0.016 [$/kWh] |

### Life cycle assessment (LCA)

The environmental performance of the integrated AEL-PRMD system was evaluated in accordance with ISO 14040/14044 standards using the ReCiPe 2016 (H) method[81,82] A gate-to-gate system boundary was adopted, including ammonia-rich wastewater input, ammonia electrolysis and hydrogen generation in the AEL unit, freshwater production and hydraulic energy recovery in the PRMD unit and the resulting output streams.

The functional unit was defined as 1 kg $H_2$-equivalent to reflect the multi-output nature of the process. Inventory data were obtained from process simulation outputs and implemented in OpenLCA using ecoinvent v3.8 datasets. Scenario-based analysis was conducted for influent ammonia concentration of 5–1000 ppm and standalone AEL, standalone PRMD and integrated AEL-PRMD configurations. Six midpoint indicators (global warming, marine ecotoxicity, freshwater eutrophication, human toxicity, ozone formation and fossil resource scarcity) and the corresponding endpoint indicators (human health, ecosystems and resources) were selected.

To assess whether process integration provides environmental benefits over standalone operation, the integrated AEL-PRMD system was compared with standalone AEL and PRMD subsystems. Direct comparison between standalone AEL and PRMD subsystems is not appropriate on a mass basis due to differences in the thermodynamic value of outputs (hydrogen vs freshwater). Therefore, an exergy-based allocation was applied[83]. This approach ensures thermodynamically consistent comparison of standalone and integrated AEL-PRMD configurations.

The specific exergy is calculated as:

$$E_x = \Delta h - T_0 \Delta s \tag{86}$$

where $E_x$ is the specific exergy of the product stream, $\Delta h$ is the enthalpy change of the product stream relative to the reference state, $\Delta s$ is the entropy change of the product stream relative to the reference state, $T_0$ is the environmental reference temperature.

The thermodynamic properties of hydrogen and freshwater were obtained from Aspen Plus.

Based on these thermodynamic properties, the exergy ratio between the AEL and PRMD product streams was determined as:

$$\frac{E_{x\,AEL}}{E_{x\,PRMD}} = 9.6 \tag{87}$$

indicating that hydrogen has approximately one order of magnitude higher useful work potential than freshwater.

Environmental impacts were therefore adjusted using:

$$LCIA^* = E_x \times LCIA \tag{88}$$

where $LCIA^*$ is the exergy-adjusted environmental impact, $LCIA$ is the life cycle impact assessment result before exergy adjustment.

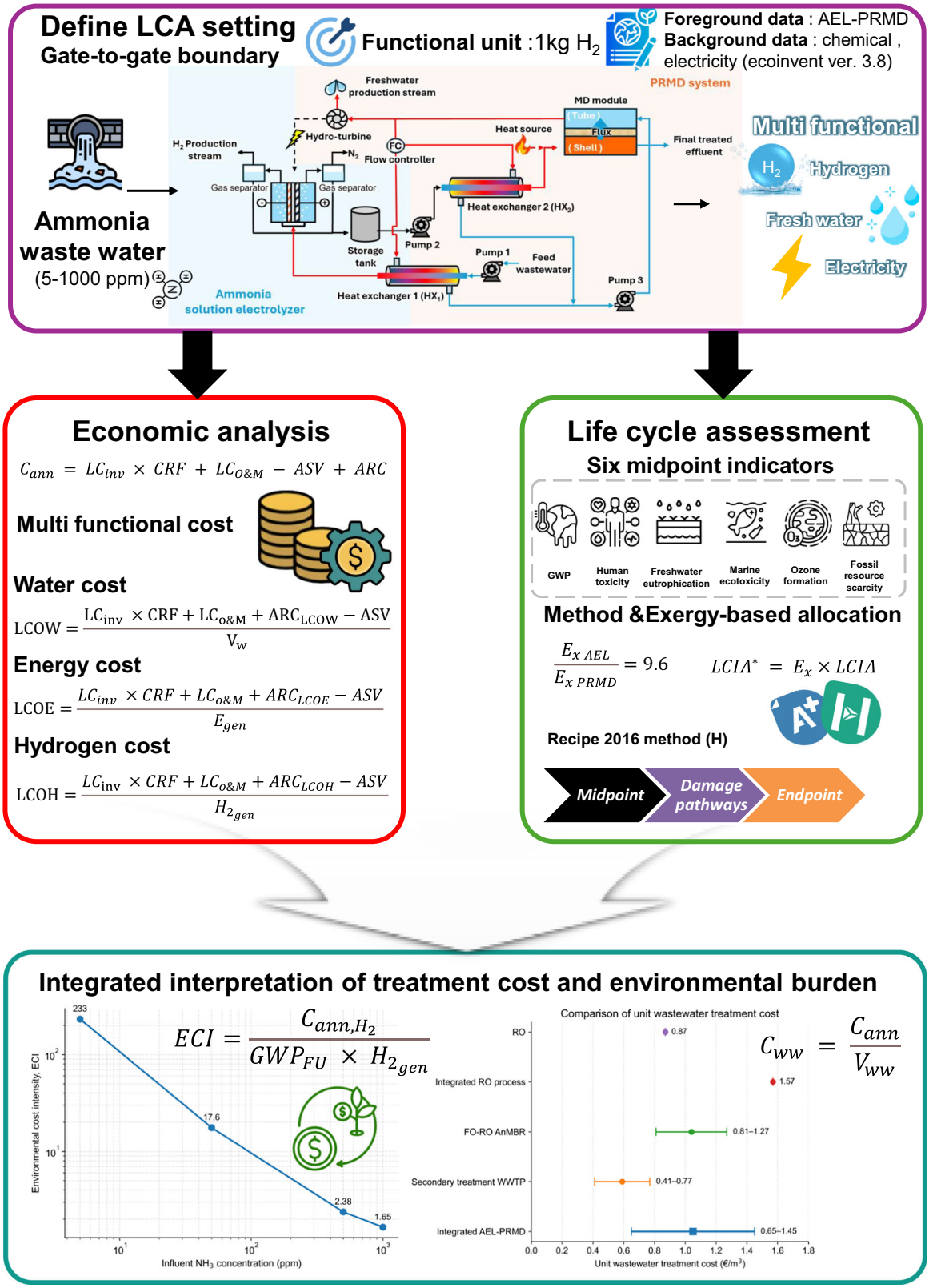



**Fig. 11 | Integrated TEA-LCA framework for evaluating the economic and environmental performance of the AEL-PRMD system.** This figure shows the overall framework used to connect the process simulation results of the integrated AEL-PRMD system with technoeconomic analysis and life cycle assessment. The gate-to-gate boundary includes ammonia-containing wastewater as the feed stream, the integrated AEL-PRMD process and multifunctional outputs including $H_2$, freshwater, and electricity. Foreground data were obtained from the AEL-PRMD process model, while background data were taken from chemical and electricity inventory data from ecoinvent ver. 3.8. The economic analysis includes water cost, energy cost and hydrogen cost. Exergy-based allocation was applied to account for the multifunctional nature of the system, and the resulting economic and environmental indicators were combined using the environmental cost intensity metric.

### Environmental cost intensity (ECI): an integrated economic-environmental metric

To interpret the trade-off between economic cost and climate impact, an environmental cost intensity (ECI) metric was introduced:

$$ECI = \frac{C_{ann,H_2}}{GWP_{ann}} = \frac{C_{ann,H_2}}{GWP_{FU} \times H_{2_{gen}}} \quad (89)$$

where $GWP_{ann}$ denotes the annual global warming burden. In the integrated AEL-PRMD system, ammonia removal is directly coupled with hydrogen generation through electrochemical decomposition. Therefore, ECI is defined on a hydrogen production basis, providing a consistent reference for evaluating both economic cost (numerator) and environmental impact (denominator). This approach focuses on ammonia removal and its associated hydrogen production, rather than representing the full scope of wastewater treatment. This formulation enables a unified comparison of the combined economic and environmental performance of the integrated AEL-PRMD system across varying influent ammonia concentrations, while reflecting the intrinsic coupling between wastewater treatment and hydrogen production. A detailed integrated TEA-LCA framework is included in Fig. 11.

## Data Availability

The datasets generated and/or analysed during the current study are not publicly available because they form part of ongoing research projects but are available from the corresponding author on reasonable request.

## Code availability

Code will be available from the corresponding author upon reasonable request.

Received: 18 April 2026; Accepted: 14 June 2026;
Published online: 30 June 2026

## References

1. Ahmed, S. F. et al. Threats, challenges and sustainable conservation strategies for freshwater biodiversity. *Environ. Res.* **214**, 113808 (2022).
2. Ministry of Environment (MOE). *Enforcement Rules of the Water Environment Conservation Act [Appendix 13]: Standards for Permissible Emissions of Water Pollutants*. *Enforcement Rules of the Water Environment Conservation Act [Appendix 13]: Standards for Permissible Emissions of Water Pollutants* (2006).
3. WHO Chronicle. *Guidelines for Drinking-Water Quality: Fourth Edition Incorporating the First Addendum*. **38**, https://apps.who.int/iris/handle/10665/254637 (2017).
4. Estejab, A., Daramola, D. A. & Botte, G. G. Mathematical model of a parallel plate ammonia electrolyzer for combined wastewater remediation and hydrogen production. *Water Res.* **77**, 133–145 (2015).
5. Sun, Z. et al. Modeling and simulation of dynamic characteristics of a green ammonia synthesis system. *Energy Convers. Manag.* **300**, 117893 (2024).
6. Madheswaran, D. K. et al. Ammonia as a hydrogen carrier: a comprehensive analysis of electrolysis efficiency and its potential in sustainable energy systems. *Renew. Sustain. Energy Rev.* **221**, 115915 (2025).
7. AlZaabi, A., AlMarzooqi, F. & Choi, D. Ammonia electro-catalysis for hydrogen production: mechanisms, materials, and scalability. *Int. J. Hydrogen Energy* **94**, 23–52 (2024).
8. Allen, J., Panquet, S. & Bastiani, A. Electrochemical ammonia: power to ammonia ratio and balance of plant requirements for two different electrolysis approaches. *Front. Chem. Eng.* **3**, 765457 (2021).
9. Rizwan, M., Alstad, V. & Jäschke, J. Design considerations for industrial water electrolyzer plants. *Int. J. Hydrog. Energy* **46**, 37120–37136 (2021).
10. Park, H. et al. Feasibility analysis of green hydrogen imports from wind power plants in Australia to South Korea. *Korean J. Chem. Eng.* **42**, 3515–3532 (2025).
11. Dawoodian, M. et al. Effects of the electrode supporter structures for achieving optimum hydrodynamic performance for a zero-gap alkaline water electrolysis cell. *Korean J. Chem. Eng*. https://doi.org/10.1007/s11814-026-00664-9 (2026)
12. Park, K., Kim, D. Y. & Yang, D. R. Theoretical analysis of pressure retarded membrane distillation (PRMD) process for simultaneous production of water and electricity. *Ind. Eng. Chem. Res.* **56**, 14888–14901 (2017).
13. Lee, M. S., Chang, J. W., Park, K. & Yang, D. R. Energetic and exergetic analyses of a closed-loop pressure retarded membrane distillation (PRMD) for low-grade thermal energy utilization and freshwater production. *Desalination* **534**, 115799 (2022).
14. Kim, H. S., Cho, G. S., Park, Y. G. & Park, K. Energy self-sustainable operation of solar-powered pressure-retarded membrane distillation: mmodeling, implementation viability, and economic feasibility study. *Desalination* **592**, 118076 (2024).
15. Sun, S. et al. Trace amount of $RuO_2$ loaded on $TiO_2$ nanowires for efficient electrocatalytic degradation of ammonia nitrogen in wastewater. *J. Alloy. Compd.* **928**, 167058 (2022).
16. Yuan, Z. et al. Pressure-retarded membrane distillation for low-grade heat recovery: the critical roles of pressure-induced membrane deformation. *J. Memb. Sci.* **579**, 90–101 (2019).
17. Kwon, J., Choi, S., Park, C., Han, H. & Song, T. Critical challenges and opportunities for the commercialization of alkaline electrolysis: high current density, stability, and safety. *Mater. Chem. Front.* **8**, 41–81 (2023).
18. Sebbahi, S. et al. A comprehensive review of recent advances in alkaline water electrolysis for hydrogen production. *Int. J. Hydrogen Energy* **82**, 583–599 (2024).
19. Jiang, M., Zhu, D. & Zhao, X. Electrolysis of ammonia for hydrogen production catalyzed by Pt and Pt-Ir deposited on nickel foam. *J. Energy Chem.* **23**, 1–8 (2014).
20. Van, V., Guerra, M. & Reis, Z. *Modelling and Experimental Validation of an Alkaline Ammonia Electrolysis Cell for Hydrogen Production* (Universidade de Lisboa, Instituto Superior Técnico, 2022)
21. Haug, P., Kreitz, B., Koj, M. & Turek, T. Process modelling of an alkaline water electrolyzer. *Int. J. Hydrog. Energy* **42**, 15689–15707 (2017).
22. Azuan, M., Yahaya, N. Z., Melinda, A. & Wasif Umar, M. Effect of temperature on performance of advanced alkaline electrolyzer. *Sci. Int.* **31**, 757–762 (2019).
23. Sakkas, N. P., Gillung, F., Thummar, K., Abang, R. & Röntzsch, L. Advanced pressurized alkaline water electrolysis at high temperatures up to 130 °C. *Int. J. Hydrog. Energy* **149**, 150075 (2025).
24. Jang, D. et al. Numerical modeling and analysis of the temperature effect on the performance of an alkaline water electrolysis system. *J. Power Sources* **506**, 230106 (2021).
25. Zhang, K. et al. Energy-efficient and cost-effective ammonia electrolysis for converting ammonia to green hydrogen. *Cell Rep. Phys. Sci.* **5**, 102171 (2024).
26. International Energy Agency. *The Future of Hydrogen*. https://www.iea.org/reports/the-future-of-hydrogen (2019).
27. Ghaffour, N., Missimer, T. M. & Amy, G. L. Technical review and evaluation of the economics of water desalination: Current and future challenges for better water supply sustainability. *Desalination* **309**, 197–207 (2013).
28. Lee, J. M. & Choi, H.-B. Development of a vertical multi-stage ammonia stripping reactor for recovering ammonia from wastewater with high nitrogen concentrations(I). *J. Korea Org. Resour. Recycl. Assoc.* **25**, 41–48 (2017).

29. Dantas, M. S., de Morais Silva, L. F., Novaes, H. H. U. & Oliveira, S. C. Municipal wastewater discharge standards for ammonia nitrogen in Brazil: Technical elements to guide decisions. *Water Sci. Technol.* **85**, 3479–3492 (2022).
30. Tang, J., Zhang, C., Shi, X., Sun, J. & Cunningham, J. A. Municipal wastewater treatment plants coupled with electrochemical, biological and bio-electrochemical technologies: opportunities and challenge toward energy self-sufficiency. *J. Environ. Manag.* **234**, 396–403 (2019).
31. Goliopoulos, N., Mamais, D., Noutsopoulos, C., Dimopoulou, A. & Kounadis, C. Energy consumption and carbon footprint of greek wastewater treatment plants. *Water* **14**, 320 (2022).
32. Wang, X. et al. Analysis of the electricity consumption in municipal wastewater treatment plants in northeast China in terms of wastewater characteristics. *Int. J. Environ. Res. Public Health* **19**, 14398 (2022).
33. Krzeminski, P., Van Der Graaf, J. H. J. M. & Van Lier, J. B. Specific energy consumption of membrane bioreactor (MBR) for sewage treatment. *Water Sci. Technol.* **65**, 380–392 (2012).
34. STOWA; Witteveen+Bos Consulting Engineers. *Membrane Bioreactors for Municipal Wastewater Treatment: State of the Science Report*. https://www.stowa.nl/sites/default/files/assets/PUBLICATIES/Publicaties%202000-2010/Publicaties%202005-2009/STOWA%202005-XX%20boek%2024.pdf (2005).
35. Woo, S. Y., Kim, J. S. & Kim, Y. D. Assessment of the suitability of adsorption water treatment as a concentration process for resource recovery and wastewater treatment. *Sep. Purif. Technol.* **335**, 126177 (2024).
36. Satyam, S. & Patra, S. Innovations and challenges in adsorption-based wastewater remediation: A comprehensive review. *Heliyon* **10**, e29573 (2024).
37. Latvytė, E. et al. A low-temperature ammonia electrolyser for wastewater treatment and hydrogen production. *Int. J. Hydrog. Energy* **52**, 265–282 (2024).
38. Jo, C. et al. Meticulous integration of N and C active sites in Ni2P electrocatalyst for sustainable ammonia oxidation and efficient hydrogen production. *Chem. Eng. J.* **463**, 142314 (2023).
39. Yang, Y. et al. A rigorous electrochemical ammonia electrolysis protocol with in operando quantitative analysis. *J. Mater. Chem. A Mater.* **9**, 11571–11579 (2021).
40. Vitse, F., Cooper, M. & Botte, G. G. On the use of ammonia electrolysis for hydrogen production. *J. Power Sources* **142**, 18–26 (2005).
41. Guo, X., Zhu, H. & Zhang, S. Overview of electrolyser and hydrogen production power supply from industrial perspective. *Int. J. Hydrogen Energy* **49**, 1048–1059 (2024).
42. Sommariva, C., Borsani, R., Butt, M. I. & Sultan, A. H. Reduction of power requirements for MSF desalination plants: the example of Al Taweelah B. *Desalination* **108**, 37–42 (1997).
43. Darwish, M. A., Yousef, F. A. & Al-Najem, N. M. Energy consumption and costs with a multi-stage flashing (MSF) desalting system. *Desalination* **109**, 285–302 (1997).
44. Grzegorzek, M., Wartalska, K. & Kaźmierczak, B. Review of water treatment methods with a focus on energy consumption. *Int. Commun. Heat. Mass Transf.* **143**, 106674 (2023).
45. Avlonitis, S. A., Kouroumbas, K. & Vlachakis, N. Energy consumption and membrane replacement cost for seawater RO desalination plants. Desalination and the environment: fresh water for all. *Desalination* **157**, 151–158 (2003).
46. McGinnis, R. L. & Elimelech, M. Energy requirements of ammonia-carbon dioxide forward osmosis desalination. *Desalination* **207**, 370–382 (2007).
47. Schwantes, R. et al. Thermally driven ultrapure water production for water electrolysis – a techno-economic analysis of membrane distillation. *Desalination* **608**, 118848 (2025).
48. Soliman, M. et al. Treatment technologies for cooling water blowdown: a critical review. *Sustainability* **14**, 376 (2022).
49. Hernández-Sancho, F. & Sala-Garrido, R. Technical efficiency and cost analysis in wastewater treatment processes: a DEA approach. *Desalination* **249**, 230–234 (2009).
50. Vinardell, S., Astals, S., Mata-Alvarez, J. & Dosta, J. Techno-economic analysis of combining forward osmosis-reverse osmosis and anaerobic membrane bioreactor technologies for municipal wastewater treatment and water production. *Bioresour. Technol.* **297**, 122395 (2020).
51. Ochando-Pulido, J., Hodaifa, G. & Victor-Ortega, M. Performance modeling and cost analysis of a pilot-scale reverse osmosis process for the final purification of olive mill wastewater. *Membranes* **3**, 285–297 (2013).
52. Motahari, A., Dana, T., Kargari, N., Monavari, S. M. & Haghighi Fard, N. J. Integrating life cycle assessment and health risk assessment of direct and indirect exposure (case study: a combined cycle power plant). *J. Clean. Prod.* **436**, 140342 (2024).
53. Farghali, M. et al. Strategies for ammonia recovery from wastewater: a review. *Environ. Chem. Lett.* **22**, 2699–2751 (2024).
54. Dong, Y., Yuan, H., Zhang, R. & Zhu, N. Removal of ammonia nitrogen from wastewater: a review. *Trans. ASABE* **62**, 1767–1778 (2019).
55. Adam, M. R. et al. Current trends and future prospects of ammonia removal in wastewater: a comprehensive review on adsorptive membrane development. *Sep. Purif. Technol*. **213**, 114–132 (2019).
56. Ren, Z. et al. Study on adsorption of ammonia nitrogen by iron-loaded activated carbon from low temperature wastewater. *Chemosphere* **262**, 127895 (2021).
57. Zangeneh, A., Sabzalipour, S., Takdatsan, A., Yengejeh, R. J. & Khafaie, M. A. Ammonia removal form municipal wastewater by air stripping process: an experimental study. *S. Afr. J. Chem. Eng.* **36**, 134–141 (2021).
58. Guillen-Burrieza, E., Moritz, E., Hobisch, M. & Muster-Slawitsch, B. Recovery of ammonia from centrate water in urban waste water treatment plants via direct contact membrane distillation: Process performance in long-term pilot-scale operation. *J. Memb. Sci.* **667**, 121161 (2023).
59. Oikonomidis, S. et al. Transient modelling of a multi-cell alkaline electrolyzer for gas crossover and safe system operation. *Int. J. Hydrog. Energy* **48**, 34210–34228 (2023).
60. Kim, H., Park, M. & Lee, K. S. One-dimensional dynamic modeling of a high-pressure water electrolysis system for hydrogen production. *Int. J. Hydrog. Energy* **38**, 2596–2609 (2013).
61. Haug, P., Koj, M. & Turek, T. Influence of process conditions on gas purity in alkaline water electrolysis. *Int. J. Hydrog. Energy* **42**, 9406–9418 (2017).
62. Chin Kwie Joe, J. M. et al. Bubble parameters and efficiency of gas bubble evolution for a chlorine-, a hydrogen-and an oxygen-evolving wire electrode. *Electrochim. Acta* **33**, 769–779 (1988).
63. Kikuchi, K., Nagata, S., Tanaka, Y., Saihara, Y. & Ogumi, Z. Characteristics of hydrogen nanobubbles in solutions obtained with water electrolysis. *J. Electroanal. Chem.* **600**, 303–310 (2007).
64. Abdin, Z., Webb, C. J. & Gray, E. M. Modelling and simulation of a proton exchange membrane (PEM) electrolyser cell. *Int. J. Hydrog. Energy* **40**, 13243–13257 (2015).
65. Henao, C., Agbossou, K., Hammoudi, M., Dubé, Y. & Cardenas, A. Simulation tool based on a physics model and an electrical analogy for an alkaline electrolyser. *J. Power Sources* **250**, 58 (2014).
66. Vogt, H. & Balzer, R. J. The bubble coverage of gas-evolving electrodes in stagnant electrolytes. *Electrochim. Acta* **50**, 2073–2079 (2005).
67. Phillips, R., Edwards, A., Rome, B., Jones, D. R. & Dunnill, C. W. Minimising the ohmic resistance of an alkaline electrolysis cell

through effective cell design. *Int. J. Hydrog. Energy* **42**, 23986–23994 (2017).
68. Allebrod, F., Mollerup, P. L., Chatzichristodoulou, C. & Mogensen, M. Electrical conductivity measurements of aqueous and immobilized potassium hydroxide. *Int. J. Hydrogen Energy* **37**, 16505–16514 (2012).
69. Niroula, S., Chaudhary, C., Subedi, A. & Thapa, B. S. Parametric modelling and optimization of alkaline electrolyzer for the production of green hydrogen. *IOP Conf. Ser. Mater. Sci. Eng.* **1279**, 012005 (2023).
70. Cha, H., Gu, B. & Jeong, S. Enhancing ammonia selectivity in membrane distillation: the role of membrane structural characteristics. *Desalination* **592**, 118059 (2024).
71. Lide, D. R. *CRC Handbook of Chemistry and Physics*, Vol. 73 (CRC Press, 1993).
72. Kim, D., Lee, H., Jeon, J. & Kim, S. High recovery design of reverse osmosis process with high permeate water quality and low wastewater discharge for ultra-pure water production. *Desalination* **592**, 118149 (2024).
73. Martínez-Díez, L. & Vázquez-Gonzàlez, M. I. Temperature polarization in mass transport through hydrophobic porous membranes. *AIChE J.* **42**, 1844–1852 (1996).
74. Alklaibi, A. & Lior, N. Heat and mass transfer resistance analysis of membrane distillation. *J. Memb. Sci.* **282**, 362–369 (2006).
75. Boubakri, A., Al-Tahar Bouguecha, S. & Hafiane, A. *Membrane Distillation Process: Fundamentals, Applications, and Challenges*. www.intechopen.com.
76. Park, K., Heo, H., Kim, D. Y. & Yang, D. R. Feasibility study of a forward osmosis/crystallization/reverse osmosis hybrid process with high-temperature operation: modeling, experiments, and energy consumption. *J. Memb. Sci.* **555**, 206–219 (2018).
77. Winter, D. et al. Comparative analysis of full-scale membrane distillation contactors - methods and modules. *J. Memb. Sci.* **524**, 758–771 (2017).
78. Huang, H., Liu, J., Zhang, P., Zhang, D. & Gao, F. Investigation on the simultaneous removal of fluoride, ammonia nitrogen and phosphate from semiconductor wastewater using chemical precipitation. *Chem. Eng. J.* **307**, 696–706 (2017).
79. Ryu, H. D., Kim, D. & Lee, S. I. Application of struvite precipitation in treating ammonium nitrogen from semiconductor wastewater. *J. Hazard. Mater.* **156**, 163–169 (2008).
80. Hu, S. et al. A comprehensive review of alkaline water electrolysis mathematical modeling. *Appl. Energy* **327**, 120099 (2022).
81. Finkbeiner, M., Inaba, A., Tan, R. B. H., Christiansen, K. & Klüppel, H. J. The new international standards for life cycle assessment: ISO 14040 and ISO 14044. *Int. J. Life Cycle Assess*. Volume **11**, 80–85 (2006).
82. Kazemi, A., Bahramifar, N., Heydari, A. & Olsen, S. I. Life cycle assessment of nanoadsorbents at early stage technological development. *J. Clean. Prod.* **174**, 527–537 (2018).
83. Gao, R. et al. A life cycle exergy-based analysis of Power-to-liquid/Power-to-gas hybrid processes coupled with different water electrolysis technologies. *Fuel* **357**, 130040 (2024).
84. Abu Hasan, H., Sheikh Abdullah, S. R., Kamarudin, S. K., Tan Kofli, N. & Anuar, N. Simultaneous NH4+-N and Mn2+ removal from drinking water using a biological aerated filter system: effects of different aeration rates. *Sep. Purif. Technol.* **118**, 547–556 (2013).
85. Jin, Y., Wang, D. & Zhang, W. Treatment of high-strength ammonia containing wastewater using partial nitritation system with biological selector. *Glob. NEST J.* **17**, 738–743 (2015).
86. Su, B. et al. Simultaneous partial nitrification, anammox, and denitrification in an upflow microaerobic membrane bioreactor treating middle concentration of ammonia nitrogen wastewater with low COD/TN ratio. *Chemosphere* **295**, 133832 (2022).
87. Zhou, X. et al. Unravelling nitrogen removal and nitrous oxide emission from mainstream integrated nitrification-partial denitrification-anammox for low carbon/nitrogen domestic wastewater. *J. Environ. Manag.* **270**, 110872 (2020).
88. Li, H. & Tao, W. Efficient ammonia removal in recirculating vertical flow constructed wetlands: Complementary roles of anammox and denitrification in simultaneous nitritation, anammox and denitrification process. *Chem. Eng. J.* **317**, 972–979 (2017).
89. Halim, A. A., Aziz, H. A., Johari, M. A. M. & Ariffin, K. S. Comparison study of ammonia and COD adsorption on zeolite, activated carbon and composite materials in landfill leachate treatment. *Desalination* **262**, 31–35 (2010).
90. Marañón, E., Ulmanu, M., Fernández, Y., Anger, I. & Castrillón, L. Removal of ammonium from aqueous solutions with volcanic tuff. *J. Hazard. Mater.* **137**, 1402–1409 (2006).
91. Cheng, H., Zhu, Q. & Xing, Z. Adsorption of ammonia nitrogen in low temperature domestic wastewater by modification bentonite. *J. Clean. Prod.* **233**, 720–730 (2019).
92. Khosravi, A., Esmhosseini, M. & Khezri, S. Removal of ammonium ion from aqueous solutions using natural zeolite: Kinetic, equilibrium and thermodynamic studies. *Res. Chem. Intermed.* **40**, 2905–2917 (2014).
93. dos Santos, H. A. P., de Castilhos Júnior, A. B., Nadaleti, W. C. & Lourenço, V. A. Ammonia recovery from air stripping process applied to landfill leachate treatment. *Environ. Sci. Pollut. Res.* **27**, 45108–45120 (2020).
94. Provolo, G. et al. Nitrogen removal from digested slurries using a simplified ammonia stripping technique. *Waste Manag.* **69**, 154–161 (2017).
95. Yuan, M. H., Chen, Y. H., Tsai, J. Y. & Chang, C. Y. Removal of ammonia from wastewater by air stripping process in laboratory and pilot scales using a rotating packed bed at ambient temperature. *J. Taiwan Inst. Chem. Eng.* **60**, 488–495 (2016).
96. Cao, L. et al. Nutrient removal from digested swine wastewater by combining ammonia stripping with struvite precipitation. *Environ. Sci. Pollut. Res.* **26**, 6725–6734 (2019).
97. Zhou, S. et al. A review of the development in shale oil and gas wastewater desalination. *Sci. Total Environ.* **873**, 162376 (2023).
98. Ahmad, M. & Williams, P. Assessment of desalination technologies for high saline brine applications - discussion paper. *Desalin. Water Treat.* **30**, 1–15 (2011).
99. Finklea, H., Lin, L. S. & Khajouei, G. Electrodialysis of softened produced water from shale gas development. *J. Water Process Eng.* **45**, 102486 (2022).
100. Rahimi-Ahar, Z., Hatamipour, M. S. & Ahar, L. R. Air humidification-dehumidification process for desalination: a review. *Prog. Energy Combust. Sci.* **80.** 100850 (2020).
101. Shalaby, S. M., Kabeel, A. E., Moharram, B. M. & Fleafl, A. H. Experimental study of hybrid solar humidification dehumidification system for extremely saline water desalination. *Energy Convers. Manag.* **235**, 114021 (2021).
102. Alhaj, M. & Al-Ghamdi, S. G. Why is powering thermal desalination with concentrated solar power expensive? assessing economic feasibility and market commercialization barriers. *Sol. Energy* **189**, 480–490 (2019).
103. Colciaghi, R., Simonetti, R., Molinaroli, L., Binotti, M. & Manzolini, G. Levelized cost of water assessment for small-scale desalination plant based on forward osmosis process. *Energy Convers. Manag.* **271**, 116336 (2022).
104. Hönig, F., Rupakula, G. D., Duque-Gonzalez, D., Ebert, M. & Blum, U. Enhancing the levelized cost of hydrogen with the usage of the byproduct oxygen in a wastewater treatment plant. *Energies* **16**, 4829 (2023).
105. Durrant, A. A., Pearson, T. G. & Robinson, P. L. Physical relationships amongst the hydrides of elements of the fifth group with special reference to association in these compounds. *J. Chem. Soc.* **8**, 730–735 (1934).

106. Nathan Osborns, B. S. & Van Dussn, M. S. Specific heat of liquid ammonia. *J. Am. Chem. Soc.* **40.1**, 1–13 (1918).
107. Makhija, R. C. & Stairs, R. A. Viscosity of associated liquids. *Can. J. Chem.* **48**, 1214–1218 (1970).
108. Keyes, F. G. & Brownlee, R. B. The vapor pressure of liquid ammonia up to the critical temperature. Part II. *J. Am. Chem. Soc.* **40**, 25–45 (1918).
109. Tham, by K., Walker, R. D. & Gubbins, K. E. *Diffusion of Oxygen and Hydrogen Diffusion of Oxygen and Hydrogen in Aqueous Potassium Hydroxide Solutions. 1 Introduction The Rate of Diffusion of Dissolved Gases in Electrolytic Solution Is an Important Consideration in Determining*. https://pubs.acs.org/sharingguidelines (American Chemical Society, 1918).
110. Cadogan, S. P., Maitland, G. C. & Trusler, J. P. M. Diffusion coefficients of $CO_2$ and $N_2$ in water at temperatures between 298.15 K and 423.15 K at pressures up to 45 MPa. *J. Chem. Eng. Data* **59**, 519–525 (2014).
111. Schalenbach, M., Lueke, W. & Stolten, D. Hydrogen diffusivity and electrolyte permeability of the Zirfon Perl separator for alkaline water electrolysis. *J. Electrochem. Soc.* **163**, F1480–F1488 (2016).
112. Feldkamp, K. Die Oberflächenspannung wäßriger NaOH- und KOH-Lösungen. *Chem. Ing. Tech.* **41**, 1181–1183 (1969).
113. Kibria, M. Electrochemical studies of a nickel electrode for the hydrogen evolution reaction. *Int. Assoc. Hydrog. Energy* **20**, 435–440 (1995).
114. Gwak, J., Choun, M. & Lee, J. Alkaline ammonia electrolysis on electrodeposited platinum for controllable hydrogen production. *ChemSusChem*. **9**, 403–408 (2016).
115. Brauns, J. & Turek, T. Model-based analysis and optimization of pressurized alkaline water electrolysis powered by renewable energy. *J. Electrochem. Soc.* **170**, 064510 (2023).
116. Jang, D., Kim, J., Kim, D., Han, W. B. & Kang, S. Techno-economic analysis and Monte Carlo simulation of green hydrogen production technology through various water electrolysis technologies. *Energy Convers. Manag.* **258**, 115499 (2022).
117. Nordio, M. et al. Techno-economic evaluation on a hybrid technology for low hydrogen concentration separation and purification from natural gas grid. *Int. J. Hydrog. Energy* **46**, 23417–23435 (2021).
118. Choi, J. et al. Performance and economic analysis of a solar membrane distillation pilot plant under various operating conditions. *Energy Convers. Manag.* **268**, 115991 (2022).
119. Li, Q. et al. An integrated, solar-driven membrane distillation system for water purification and energy generation. *Appl. Energy* **237**, 534–548 (2019).


## Acknowledgements

This work was supported by the Gwangju Green Environment Center (Grant No. 24-03-10-13-12). The authors thank Gwangju Green Environment Center for granting permission to publish this article. This work was also partly supported by the National Research Foundation of Korea (NRF) grant funded by the Korea government(MSIT) (RS-2024-00347319).

## Author contributions

All authors (S.O., H.S.K., K.P. and B.G.) contributed to the conceptualisation of this study. S.O. conducted the process modelling and energy analysis, while H.S.K. performed the technoeconomic analysis (TEA) and life cycle assessment (LCA). S.O. and H.S.K. jointly prepared the manuscript. K.P. and B.G. supervised the research, contributed to the interpretation of results, and provided critical revisions to the manuscript. All authors have reviewed and approved the final version of the manuscript and agree to be accountable for their contributions, ensuring that any questions related to the accuracy or integrity of any part of the work are appropriately investigated and resolved.

## Competing interests

The authors declare no competing interests.

## Additional information

**Supplementary information** The online version contains supplementary material available at https://doi.org/10.1038/s41545-026-00599-y.

**Correspondence** and requests for materials should be addressed to Kiho Park or Boram Gu.

**Reprints and permissions information** is available at http://www.nature.com/reprints

**Publisher's note** Springer Nature remains neutral with regard to jurisdictional claims in published maps and institutional affiliations.

**Open Access** This article is licensed under a Creative Commons Attribution-NonCommercial-NoDerivatives 4.0 International License, which permits any non-commercial use, sharing, distribution and reproduction in any medium or format, as long as you give appropriate credit to the original author(s) and the source, provide a link to the Creative Commons licence, and indicate if you modified the licensed material. You do not have permission under this licence to share adapted material derived from this article or parts of it. The images or other third party material in this article are included in the article's Creative Commons licence, unless indicated otherwise in a credit line to the material. If material is not included in the article's Creative Commons licence and your intended use is not permitted by statutory regulation or exceeds the permitted use, you will need to obtain permission directly from the copyright holder. To view a copy of this licence, visit http://creativecommons.org/licenses/by-nc-nd/4.0/.

© The Author(s) 2026